Flow, Turbulence and Combustion
https://doi.org/10.1007/s10494-024-00590-y

RESEARCH

A Reformulation of the Laminar Kinetic Energy Model to Enable Multi-mode Transition Predictions

Roberto Pacciani[1] · **Yuan Fang**[2] · **Leonardo Metti**[1] · **Michele Marconcini**[1] · **Richard Sandberg**[2]

Received: 19 April 2024 / Accepted: 25 September 2024

Abstract

The paper describes the development of a novel transition/turbulence model based on the laminar kinetic energy concept. The model is intended as a base framework for data-driven improvements. Starting from a previously developed framework, mainly aimed at separated-flow transition predictions, suitable terms for model generalization are identified and reformulated for handling different transition modes, namely bypass and separated-flow modes. The ideology for the definition of new terms has its roots in mixing phenomenological and correlation-based arguments, ensuring generality and flexibility and allowing a variety of lines of action for improving model components via machine-learning approaches. The model calibration, carried out with reference to flat plate test cases subjected to different pressure gradients and freestream turbulence levels, is discussed in detail. Although the constructed model is calibrated on a group of classic flat plat cases, the validation campaign, mostly carried out on gas turbine cascades, demonstrates its ability to predict transitional flows with engineering accuracy. Finally, while the model is not specifically developed for natural transition predictions, satisfactory predictions are obtained in scenarios with low freestream turbulence for flat plate and airfoil flows.

Keywords Laminar-turbulent multi-mode transition · Laminar kinetic energy · Data-driven transition modelling

1 Introduction

The capability of predicting transition from laminar to turbulent flow is of crucial importance for the design of fluid systems and their components, ranging from external aerodynamics to turbomachinery flows in the contexts of ground, air or marine transportation, power generation, and industrial applications in general. Unfortunately, the complex and intriguing nature of the involved flow mechanisms poses serious challenges to the physical understanding and modelling of these phenomena. One of the major difficulties is represented by the variety of modes transition can be driven by, namely natural, bypass, or

---

Yuan Fang, Leonardo Metti, Michele Marconcini and Richard Sandberg have contributed equally to this work.

Extended author information available on the last page of the article separated-flow modes. Usually, the dominant flow mechanism cannot be identified a priori, and sometimes different modes can be found to interact with each other giving rise to a mixed character of the transition physics (Durbin 2017). Wall shear stress and heat transfer rate increase significantly when a transition occurs so that drag forces, total pressure losses, and thermal loadings are affected. Then, from an engineering perspective, the inaccuracy in predicting transition translates to added uncertainty concerning the performance and durability of components.

With the fast-pacing development of high-performance computing resources, high-fidelity simulations, like large-eddy (LES) or direct numerical simulations (DNS) have become feasible (Brinkerhoff and Yaras 2015; Sandberg et al. 2015; Michelassi et al. 2015; Wheeler et al. 2016; Lardeau et al. 2007). As fundamental research tools, they have contributed to shed light into the details of the transition process on a variety of engineering relevant flow configurations. However, high-fidelity simulations are still not viable for industrial design iterations, due to the high computational cost (Sandberg and Michelassi 2019). Thus, as of today and probably for the next decade, industrial design strategies are going to keep on relying on steady or unsteady Reynolds-averaged Navier–Stokes (RANS/URANS) methods, as they are cost-effective flow modelling tools for engineering solutions.

Nowadays, the majority of industrial computational fluid dynamics (CFD) approaches relies on transition models belonging to two different families: one based on the intermittency concept, and the other one based on the laminar kinetic energy (LKE) concept. A comprehensive review of the current models for turbomachinery applications has been provided by Dick and Kubacki (2017). Intermittency-based models are conceived as a general framework to include correlation-based transition criteria in RANS/URANS solvers, overcoming the difficulties associated with the use of non-local quantities. Driven by the popularity of the $\gamma - \tilde{Re}_{\theta,t}$ framework, proposed by Menter et al. (2006), a number of algebraic and transport models that exploit the flexibility of the local correlation-based modelling approach have been recently proposed (e.g. Menter et al. 2015, Ge et al. 2014, Kubacki et al. 2020, Li et al. 2021). Recently, the LKE concept has also become popular as a transition modelling framework. The LKE-based methodologies are able to address the rise of pre-transitional fluctuations in boundary layers and their subsequent breakdown to turbulence. Walters and Leylek (2004); Walters and Cokljat (2008), and Lardeau et al. (2007) exploited the LKE concept, originally introduced by Mayle and Schulz (1997), to create transition-sensitive turbulence closures based on two-equation models. Examples of successful applications of the LKE approach to turbomachinery flows have been provided by Lardeau and Leschziner (2006) and Pacciani et al. (2011b). In the latter case, a novel formulation for the LKE transport equation was proposed in order to predict separated-flow transition in highly loaded cascades. Aiming at a more general phenomenological transition modelling framework, Lopez and Walters (2016) have recently introduced the $v^2 - k - \omega$ model. It is basically a reformulation of the model by Walters and Cokljat (2008) where the laminar kinetic energy is replaced by the term v^2 which has different physical meanings depending on the boundary layer status. It represents pretransitional, wall-normal, velocity fluctuations in laminar boundary layers and three-dimensional velocity fluctuations in turbulent ones. It bears a relationship with pressure-strain interaction terms and this contributes to adding more physics in transition modelling frameworks relative to LKE-based approaches. Akolekar et al. (2019) report a fairly good performance of the model in predicting separated flow transition on a high-lift cascade (T106A) operating in low pressure turbine conditions.

The field of data-driven turbulence and transition modeling has recently gained momentum as a promising pathway for improving closures and narrowing the gap between the accuracy of high-fidelity simulations or experimental data and RANS/URANS calculations. Using some forms of machine learning, high-fidelity datasets can be mined to extract relevant physics-based insights for improving transition and turbulence models. Transport models based on a single equation are obviously preferable as transition closures for such approaches. Mainly targeted at turbomachinery flow predictions, the works by Akolekar et al. (2022); Fang et al. (2024) have shown how machine learning strategies based on the Gene Expression Programming (GEP) technique, driven by high-fidelity simulation or experimental results, are capable of generating improved closure relations in the form of symbolic regression formulas that are physically interpretable. In an effort to extend the range of applicability of the LKE model by Pacciani et al. (2011a, 2011b, 2012), aiming at a multi-mode transition modelling framework, Fang et al. (2024) found opposite correction trends in the training of model terms for separated-flow and bypass transition. This suggested a lack of generality of the baseline model and the urgency of the work described in this paper.

In the present contribution, the construction of a multi-mode LKE-based transition/turbulence closure is discussed. Starting from the original formulation reported in Pacciani et al. (2011a, 2011b, 2012), the production term of the LKE transport equation is modified in a form that comprises two contributions aimed at addressing different transition modes. The first term addresses the growth of pre-transitional fluctuations in favorable and adverse pressure gradients under the effects of the turbulence coming from the freestream, thus allowing bypass transition predictions. The second one is a separation-aware term aimed at mimicking the growth of instabilities in separated shear-layers, thus allowing separated-flow transition predictions. A boosting term for the turbulent kinetic energy (TKE) production by the turbulence model is also provided in order to allow the prediction of realistic reattachment location of laminar separation bubbles. The selected turbulence closure is based on the $k-\omega$ SST model (Menter 1994) which is coupled to the LKE transport equation via an energy transfer term and a suitably defined intermittency factor based on LKE. A laminar fluctuation diffusivity is introduced as it is found to allow an improved reproduction of the transition length in favorable pressure gradient conditions. To facilitate further data-driven improvements, the model formulation is kept as simple as possible, with the use of a limited number of closure functions. Such functions are the principal candidates for machine-learnt modifications. Although the LKE concept is considered a suitable choice for the construction of phenomenological transition closures, in its present form, the model presented herein borrows some ingredients from local correlation approaches, for the purpose of enhancing its generality and flexibility. It makes use of local quantities only, but is not Galilean invariant. As the model is mainly aimed at aerodynamic applications, this is not considered a major drawback for the moment.

After a brief recall of the baseline formulation, mainly aimed at pointing out its major drawbacks, the various terms introduced for generalizing the model will be discussed in detail and their respective roles in addressing different transition modes will be highlighted. Insights concerning a data-driven training of those terms will also be provided. The complete formulation of the new model is reported in Appendix A. Then, the model calibration is carried out with reference to the flat plate experiments by the European Research Consortium on Flow, Turbulence and Combustion (ERCOFTAC) (Pironneau et al. 1992) due to their widespread use as test cases for transition model development. Followed by the a posteriori validation of the model framework focusing on steady flow configurations past gas turbine cascades and a wind turbine airfoil, all characterized by a dominant transition mode, namely bypass, separated-flow, and natural transition. Specifically, the model capabilities for predicting bypass transition are assessed against the VKI-LS89 test case, a linear cascade representative of a high-pressure turbine stator vane. Two high-lift cascades for aeronautical low-pressure turbine applications are studied, in low Reynolds number conditions, to check for the model capabilities in predicting separated-flow transition. They are based on the T106 and T108 blade sections. Finally, calculations on the S809 airfoil are presented. This airfoil was specifically conceived for wind turbine applications and a detailed experimental campaign was carried out in realistic flow conditions characterized by a low freestream turbulence level (Somers 1997). Although this work is mainly targeted at turbomachinery flows, that are usually characterized by bypass or separated-flow transition, it was considered interesting to challenge the model generality by including a low freestream turbulence test case in the validation campaign. For every case, the grid structure was selected on the basis of previous experiences and the presented results are all space-converged as confirmed by grid dependency analyses not reported in this work for the sake of conciseness. It will be shown how the proposed transition/turbulence closure consistently yields promising results for a variety of engineering relevant flow configurations affected by different transition mechanisms.

2 Computational Framework

The transitional modelling framework was implemented in the TRAF code (Arnone 1994) that was then used for all the calculations presented in the paper. It is a state-of-the-art, in-house developed, density-based, RANS/URANS solver. Incompressible flows are handled via the artificial compressibility method proposed by Chorin (1967). In terms of numerical fluxes, a formally third-order Total Variation Diminishing (TVD) framework, based on the generalized min-mod limiter (Pacciani et al. 2019), built on top of the Roe upwind scheme, was employed.

3 Previous LKE Model

3.1 Laminar Kinetic Energy Framework

As mentioned in the Introduction section, the baseline LKE-based model adopted in the present work is the one proposed by Pacciani et al. (2011a, 2012), which was originally developed aiming at separated-flow transition. The modelled transport equation for the LKE is devised as:

$$\frac{Dk_\ell}{Dt} = P_\ell - R - D_\ell + \frac{\partial}{\partial x_j}\left(\nu \frac{\partial k_\ell}{\partial x_j}\right) \tag{1}$$

The original formulation by Mayle and Schultz was retained in Eq. (1) for the dissipation term:

$$D_\ell = 2\nu \frac{k_\ell}{y^2} \tag{2}$$

Lardeau et al. (2007) argued that, in attached and separated shear layers, the amplification of fluctuations is due more to conventional shear-stress/strain interaction rather than to pressure diffusion, like in Mayle and Schulz 1997. Hence, a model of the production of the LKE is proposed in a form that resembles a turbulent source term as:

$$P_\ell = c_1 \ell_{scale} v_{scale} S^2 \tag{3}$$

In Eq. (3), ℓ_{scale} is a characteristic length scale for pre-transitional fluctuations, v_{scale} is a suitable velocity scale, and c_1 is a model constant.

In Pacciani et al. (2011a, 2011b, 2014) the square root of the LKE was assumed as a velocity scale, while the separated shear layer vorticity thickness was used as a length scale to address the growth of Kelvin-Helmholtz (KH) instabilities.

The LKE transport equation Eq. (1) was coupled with the Wilcox $k-\omega$ model (Wilcox 2006) to obtain a transition-sensitive turbulence closure. The three transport equations of the model are written as:

$$\frac{Dk_\ell}{Dt} = P_\ell - R - D_\ell + \frac{\partial}{\partial x_j}\left(\nu \frac{\partial k_\ell}{\partial x_j}\right) \tag{4}$$

$$\frac{Dk}{Dt} = P_k + R - D_k + \frac{\partial}{\partial x_j}\left[\left(\nu + \frac{\nu_T}{\sigma_k}\right)\frac{\partial k}{\partial x_j}\right] \tag{5}$$

$$\frac{D\omega}{Dt} = P_\omega - D_\omega + \frac{\partial}{\partial x_j}\left[\left(\nu + \frac{\nu_T}{\sigma_\omega}\right)\frac{\partial \omega}{\partial x_j}\right] \tag{6}$$

The production terms for turbulent kinetic energy k and specific dissipation rate ω are:

$$P_k = \nu_T S^2, \quad P_\omega = \alpha \frac{\omega}{k} P_k \tag{7}$$

and the corresponding dissipation terms:

$$D_k = \beta^* k\omega, \quad D_\omega = \beta\omega^2 \tag{8}$$

Standard values were assumed for the model constants: α, β, and β^* (see Wilcox 2006). The eddy viscosity is defined as: $\nu_T = \alpha^* \frac{k}{\omega}$, where α^* is a damping term based on the turbulent Reynolds number: $R_T = \frac{k}{\nu\omega}$. The role of such a damping function is twofold: provide the correct asymptotic behavior of the model near solid boundaries, and ensure laminar flow prior to transition.

The R term serves as an energy transfer term from the laminar fluctuations to the turbulence field, and it is used to couple the LKE transport equation with the turbulence model. It appears in both the laminar and turbulent kinetic energy equations, but with opposite signs, resulting in no net change of the total fluctuating kinetic energy $k_{tot} = k_\ell + k$. Transition is triggered by the energy transfer from k_ℓ to k. Following (Walters and Leylek 2004) the transfer term is formulated as:

$$R = c_3 f_t k_\ell \omega, \quad f_t = \left(1 - e^{-\frac{\psi}{c_4}}\right), \quad \psi = \max\left(\frac{\sqrt{k}y}{\nu} - c_5, 0\right) \tag{9}$$

The quantity ψ can be viewed as a transition triggering function, transition occurs when the wall-distance Reynolds number $\frac{\sqrt{k}y}{\nu}$ reaches the threshold value c_5.

3.2 Model Performance and Weaknesses

The baseline LKE model was successfully applied to the prediction of separated-flow transition in LPT cascades for aircraft engine applications by Pacciani et al. (2010, 2011a, 2011b, 2014). Blade sections with different solidities and loading styles were studied over a range of Reynolds numbers and the numerical predictions resulted in separation bubble lengths, transition onset locations, and pressure recovery after reattachment that were found to be in good agreement with experimental data. However, the formulation of the production term based on k_ℓ and shear-layer vorticity thickness has some major drawbacks. First of all, this latter quantity is a non-local one, and this seriously limits the generalizability of the model. Second, the proposed expression for P_ℓ does not account for the freestream turbulence level, and while being suitable for modelling the growth of instabilities in separated shear layers, it bears a loose relation with pre-transitional fluctuations developing in attached boundary-layers (Tollmien-Schlichting waves and Klebanoff streaks). Similarly, the expression adopted for the transfer term R is not free from criticism. Generally speaking, the transition onset depends on Reynolds number, pressure gradient, and freestream turbulence intensity. From this point of view, the adoption of a constant value (the c_5 term in the ψ function) as transition onset parameter appears as a too crude assumption. Generalizations of the LKE framework were attempted, with the aid of data-driven machine learning approaches, by Akolekar et al. (2021, 2022) and Fang et al. (2024), where the production and transfer terms were chosen for model modification. Further improvements in separation-induced transition predictions were achieved, however, Fang et al. (2024) who exploited a multi-objective multi-case machine learning algorithm, found opposite correction trends on separated-flow and bypass transition by analyzing the trained LKE production and transfer terms. This reinforced the idea that the construction of a truly multi-mode LKE-based model requires a more general framework that is able to address the growth of pre-transitional fluctuations in favorable and adverse pressure gradients under the effects of the turbulence coming from the freestream.

Based on the above discussion, the weaknesses of the previous LKE model can be summarized as:

- It is a non-local model due to the use of the shear-layer vorticity thickness
- It contains no specific term for bypass transition
- The threshold constant c_5 should actually be a function of pressure gradient and freestream turbulence intensity
- The use of turbulence damping functions results in an unsatisfactory coupling with the turbulence model

In the following sections of the paper the research questions raised by the highlighted deficiencies of the previous LKE model will be addressed by:

- Reformulating the LKE production term to sensitize the model to the turbulence coming from the freestream
- Considering also a laminar fluctuations diffusivity to be included in the diffusion terms of the momentum and energy equations
- Introducing an intermittency factor to damp the TKE production term prior to transition and guarantee an effective coupling between the LKE and the turbulence model equations

- Considering suitable functional forms for the threshold term c_5
- Reformulating the separated flow transition components in order to avoid the use of non-local quantities in any model term, and address the common problem met in linear turbulence models that need boosted TKE production to overcome overpredicted reattachment lengths.

4 Reformulated LKE Framework

4.1 Laminar Kinetic Energy Production Term

Starting the discussion from the LKE production term, the adopted analytical formulation is again the one of Eq. (3). The efforts described in Akolekar et al. (2021, 2022) pointed out how the length scale:

$$\ell = \frac{\Omega y^2}{U} \tag{10}$$

or its variant with the strain rate S in place of the vorticity magnitude Ω, frequently appears in trained expressions of the LKE production terms. It is a local term that presents a maximum in the normal-to-the-wall direction which is roughly proportional to the boundary layer momentum thickness. The maximum location is approximately found at half the boundary-layer thickness in attached boundary layers, while it sits on the outer shear layer of laminar separation bubbles. This has been verified by analyzing normal-to-the-wall distributions of the term ℓ for Falkner-Skan velocity profiles. Such properties suggest that ℓ can be considered as a good candidate to represent the length scale of pre-transitional fluctuations. Note that the model is likely to initiate transition where ℓ reaches its maximum value and this appears as a physically consistent circumstance for both attached and separated-flow transition. The only drawback of the adoption of such a length scale comes from its non-Galilean-invariant character, due to the involvement of the local velocity magnitude U. However, it has been verified that its behaviour in the boundary layer is not altered when considering the flow velocity in the frame of reference of each solid wall comprised in the computational domain.

The square root of k_ℓ as a velocity scale does not account for the energy associated with fluctuations coming from the freestream and must be dropped in favor of a more physically sound term, in order to properly include the effect of freestream turbulence. Walters and Leylek (2004) and Walters and Cokljat (2008) assumed that LKE production is driven by large scale fluctuations occurring in the normal-to-the-wall direction due to turbulence coming from the freestream. They split the TKE into two contributions: a small scale term $k_{T,s}$ associated with high frequency turbulent fluctuations, and a large scale term $k_{T,l}$ associated with low frequency fluctuations penetrating into the boundary layer. The splitting is carried out on the base of a shear-sheltering function (Jacobs and Durbin 1998; Walters and Cokljat 2008):

$$f_{SS} = e^{-\left(\frac{c_{SS}\nu\Omega}{k}\right)^2} \tag{11}$$

which is used to filter out small scale fluctuations and prevent them from penetrating the pre-transitional boundary layer. Thus:

$$k_{T,s} = f_{SS}k, \quad k_{T,l} = k - k_{T,s} \tag{12}$$

It is an established physical fact and a common assumption (see also Walters and Cokljat, (2008) Dick and Kubacky, (2017)) that large-scale fluctuations coming from the free stream are responsible for the growth of pretransitional fluctuations in laminar boundary layers, while small-scale fluctuations feed turbulence in turbulent boundary layers. Along these lines, $\sqrt{k_{T,l}}$ has been assumed as a pre-transitional fluctuating velocity scale in the present work. The resulting expression for the LKE production term is:

$$P_\ell = c_1 \left(\frac{\Omega y^2}{U} \right) S^2 \sqrt{k_{T,l}} \tag{13}$$

where a value of 2 has been assumed for the constant c_{SS} in Eq. (11). The effect of the value of the c_1 constant will be discussed in section 5.

4.2 Intermittency Factor

A modified LKE model including the production term of Eq. (13) was coupled with the $k - \omega$ SST model and applied for bypass transition predictions in the ERCOFTAC flate plate test cases. The particular choice for the turbulence model is justified by its more reliable response to the freestream turbulence intensity relative to the Wilcox $k - \omega$. This aspect will be made clearer in subsection 6.1 where numerical results on the VKI-LS89 cascade will be discussed. The ERCOFTAC flat plate test cases will be analyzed in detail in sect. 5, and here only results from the T3A configuration are presented in order to discuss the failure that was experienced when applying the baseline model for bypass transition predictions. Figure 1 reports the calculated and experimental flat plate skin friction distributions $c_f = 2\tau_w / \rho U_\infty^2$ versus $Re_x = \frac{\rho U_\infty x}{\nu}$, where τ_w is the wall shear stress, x is the coordinate running along the flat plate, and U_∞ indicates the freestream flow velocity. Results obtained with the $\gamma - Re_{\theta,t}$ model (Menter et al. 2006) are also reported for comparison. The erratic

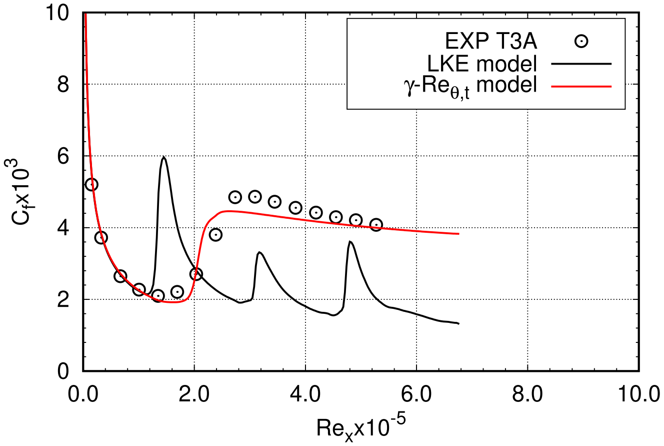

Fig. 1 Skin-friction distributions for the T3A test case (using original LKE model)

behavior of the skin friction coefficient, which clearly indicates a failure of the transition model, was found to stem from the coupling strategy between the LKE framework and the turbulence model. In bypass transition cases, the damping function $\alpha^*(R_T)$ does not allow the turbulence model to be properly ignited by the transfer term, and prevents reaching fully-turbulent flow in the boundary layer. Instead, we obtain a non-physical series of re-laminarizations and re-transitions. Several formulations were considered for $\alpha^*(R_T)$, including rational and exponential functions, but none of them were able to address the issue.

Intermittency-based models, on the other hand, are not affected by such problems. They are able to preserve laminar flow prior to transition, while ensuring a smooth increase in TKE up to the fully turbulent regime (see Fig. 1). The introduction of an intermittency factor in the LKE framework was therefore considered.

In the context of LKE-based transition models, an intermittency factor can be defined as: $\gamma = k/(k_\ell + k)$ (Lardeau and Leschziner 2006; Pacciani et al. 2024). In the pre-transitional portion of the boundary layer, only k_ℓ can be present while k is practically equal to zero, as is γ. When transition occurs k starts to increase, while k_ℓ decreases due to the effect of the transfer term, so γ approaches the unity value as the flow tends to become fully turbulent. In accelerating laminar boundary layers k_ℓ can be very small and comparable or lower than the k level established by the diffusion of freestream turbulence. This could result in γ values close to unity and then promote TKE production prior to transition. To prevent this, the kinetic energy of small scale turbulent fluctuations is employed in place of k:

$$\gamma = \frac{k_{T,s}}{k_\ell + k_{T,s}} \tag{14}$$

The kinetic energy of the high frequency turbulent fluctuations $k_{T,s}$ is filtered out in laminar boundary layers while it becomes equal to k when the fully turbulent regime is achieved.

With the introduction of the intermittency factor, the coupling of the LKE transport equation with the turbulence model can be carried out with commonly adopted strategies (e.g. Menter et al. 2006; 2015, Kubacki et al. 2020). With reference to the $k-\omega$ SST model, the coupled transition and turbulence equations can be written as:

$$\frac{Dk_\ell}{Dt} = \tilde{P}_\ell - R - D_\ell + \frac{\partial}{\partial x_j}\left(\nu \frac{\partial k_\ell}{\partial x_j}\right) \tag{15}$$

$$\frac{Dk}{Dt} = \tilde{P}_k + R - \tilde{D}_k + \frac{\partial}{\partial x_j}\left[\left(\nu + \frac{\nu_T}{\sigma_k}\right)\frac{\partial k}{\partial x_j}\right] \tag{16}$$

$$\frac{D\omega}{Dt} = P_\omega - D_\omega + \frac{\partial}{\partial x_j}\left[\left(\nu + \frac{\nu_T}{\sigma_\omega}\right)\frac{\partial \omega}{\partial x_j}\right] + CD_{k\omega} \tag{17}$$

with:

$$\tilde{P}_\ell = (1-\gamma)P_\ell \quad \tilde{P}_k = \gamma P_k, \quad \tilde{D}_k = \max(\gamma, 0.1)D_k \tag{18}$$

The $(1-\gamma)$ term is introduced in the LKE production term in order to enforce k_ℓ and R to go rapidly to zero after transition. The other quantities in equations 16 and 17 as well as the eddy viscosity are formulated, in the standard manner, like in Menter et al. (2015). It is worth noticing how such a coupling method is actually general and can be adopted with any two-equation turbulence model, for example the standard Wilcox $k-\omega$ model (Wilcox 2006).

The intended strategy for simulating the transition process is the following:

- The transition onset is controlled by the transfer of fluctuating energy from the laminar to the turbulent form and this task is operated by the R term of Eq. 1
- Once the turbulence model has been ignited with such a mechanism (i.e. the production of TKE has started due to the effect of R and γ has started to rise above zero), the transfer term rapidly decays together with k_ℓ, and the turbulent production is controlled by the intermittency factor γ that ensures a gradual increase of the TKE up to the fully turbulent regime.

4.3 Laminar Fluctuations Diffusivity

It is expected that the large scale fluctuations occurring in the normal-to-the wall direction, in the pre-transitional boundary layer, that are modelled in terms of LKE, contribute with added diffusivity. Based on this consideration, a diffusivity of laminar fluctuations was considered in the present work. Its definition is consistent with the adoption of the term ℓ as a length scale for laminar fluctuations:

$$\mu_\ell = c_{\mu,\ell} f_{\mu,\ell} \rho \ell \sqrt{k_\ell} \quad f_{\mu,\ell} = 1 - e^{R_T^{2.5}} \tag{19}$$

where $c_{\mu,\ell}$ is a constant, $R_T = \rho k/(\mu\omega)$ is the turbulent Reynolds number, and $f_{\mu,\ell}$ is a damping function that prevents μ_ℓ from affecting the viscous sublayer. This laminar eddy viscosity is added to the turbulent viscosity in the diffusive terms of the Navier–Stokes equations. Its role in the modelling of transition onset and development will be discussed in section 5.

4.4 Pressure Gradient Parameters for c_5 Formulations

The experience collected with the original LKE model, and the successive machine-learned variants, suggests that the transition onset parameter c_5 should not be a constant, but it should be treated as a function of pressure gradient and freestream turbulence level for the sake of generality. In particular, the pressure gradient imposed by the freestream has been recognized to play a major role. Recently, several strategies have been proposed to define non-dimensional local pressure gradient parameters suitable for being used in transition modelling frameworks (e.g. Menter et al. 2015, Coder and Maughmer 2012). The pressure gradient parameter introduced by Menter et al. (2015) is designed to approximate the Thwaites' parameter:

$$\lambda_\theta = -\frac{\theta^2}{\nu}\frac{1}{U}\frac{\partial p}{\partial s} \tag{20}$$

in the middle of the boundary layer. It is defined as:

$$\lambda_{\theta L} = -7.57 \times 10^{-3} [\nabla(\mathbf{U}\cdot\mathbf{n})\cdot\mathbf{n}]\frac{y^2}{\nu} + 0.0128 \tag{21}$$

where $\mathbf{n}$ represents the wall normal unit vector. Such a formulation shows several advantages, e.g. it has the desired behaviour in the boundary layer, it is based on only local quantities, and it is Galilean invariant. However, close to corners between two or more solid walls additional implementation logic could be needed. In the present work, another pressure gradient parameter, which again closely resembles λ_θ is proposed:

$$f_{PG} = \frac{y}{\nu S}\frac{\partial p}{\partial s} \tag{22}$$

It is also defined in terms of local parameters only, but it is not Galilean invariant due to the streamwise pressure derivative. The quantity f_{PG} is found to increase monotonically with the wall distance and becomes very large in the freestream. It must be stressed that this parameter has not been introduced only to offer an alternative to formulations proposed by other researchers, but to enable the model terms to properly react to different pressure gradient parameters. This is deemed to be important for closures that are aimed at data-driven generalizations.

4.5 Modification for Separated-Flow Transition

When laminar separation occurs, the response of the turbulence model to the onset of transition tends to be delayed and this results in boundary layer reattachment occurring too far downstream. This, depending on Reynolds number and freestream turbulence level, can lead to predicted bubble sizes that are larger than measured ones. This is a well-known issue that has been documented for a variety of transition closures and turbulence models (Menter et al. 2006, Pacciani et al. 2011b, Kubacki et al. 2020). The original LKE model was not affected by similar drawbacks, essentially due to the particular production term that was conceived focusing on KH instabilities. The present baseline model indeed shows the discussed undesirable behaviour in laminar separation bubbles, indicating that it needs additional terms to address the amplification of instabilities in the separated shear-layer and their subsequent breakdown to turbulence. To this end, both the production and the transfer terms are modified with the inclusion of separation-aware terms:

$$P_\ell = c_1\left(\frac{\Omega y^2}{U}\right)S^2\sqrt{k_{T,l}} + f_{sep}P_{sep} \tag{23}$$

$$P_{sep} = \max(c_{sep}\mu - \mu_T, 0)S^2 \tag{24}$$

$$R = c_3(f_t + 3c_{sep}f_{sep})k_\ell\omega \tag{25}$$

The function f_{sep} is meant to control the activation of production and transfer term components that model the growth of instabilities in separated shear layers. The formulation proposed herein has been designed to resemble the analogous terms in the Menter et al. (2015) and Kubacki et al. (2020) models:

$$f_{sep} = 1 - e^{\left[-\max\left(\frac{Re_v}{R_{cr}}-1,0\right)\right]} \tag{26}$$

where c_{sep} is a model constant, $Re_v = \frac{Sy^2}{\nu}$ is the vorticity Reynolds number and R_{cr} is a critical parameter that acts as a threshold for the activation of f_{sep}. The first attempts at predicting separated-flow transition on flat plates and low Reynolds number flows in gas turbine cascades suggested that R_{cr} should not be a constant, but again a function of pressure gradient and freestream turbulence. Since a prominent role of the non-dimensional group $r = \frac{Sy}{U}$ was observed in the expressions of machine-learnt threshold terms (e.g. Akolekar et al. 2021; 2022, Fang et al. 2024), the proposed expression for R_{cr} is based on such a quantity:

$$R_{cr} = 800 \max\left[\min(2r, 8), 1\right] \tag{27}$$

The non-dimensional group r can be regarded as a shape function. It accounts for the pressure gradient and provides a suitable scaling for Re_v in laminar separated shear layers. The function f_{sep} is also used to drive the boosting of the transfer term R by the quantity $3c_{sep}f_{sep}$. In practice, the source term addresses the growth of k_ℓ in the separated shear layer, while the additional term in R contributes to transfer the pre-transitional fluctuating energy to the turbulence field in an amplified manner, so that the turbulence model promptly reacts to transition, ensuring that breakdown and reattachment occur at realistic distances from the transition onset location.

The proposed formulation for f_{sep} will be proven to be quite effective (subsection 6.2), but it has no ambition of generality. Instead, the function f_{sep} is definitely a candidate for data-driven training in machine learning strategies, e.g. the ones employed in Akolekar et al. (2022) and Fang et al. (2024).

The quantity P_{sep} (equation 24) acts as a source term to model the growth of instabilities in the separated shear layers. It is borrowed from the Menter et al. (2015) intermittency-based model, where it is used for a more general purpose, i.e. to compensate for the retarded activation of the turbulence model sometimes observed when transition occurs under low freestream turbulence conditions. Kubacki et al. (2020) also used a source term proportional to the molecular viscosity μ and the square of the strain-rate S^2 as a TKE boosting term with a role in separated-flow transition. However, the combination of laminar and turbulent viscosity that appears in Eq. (24) has been preferred due to its self-destructing nature that comes into play when a fully turbulent regime is attained. In aerodynamic flows, the vorticity Reynolds number can become very high immediately downstream of trailing edges due to the concurrent impact of increasing wall distance and the high vorticity/strain-rate that exists in the near-wake. This could lead to persistence of large-value source and transfer terms downstream of trailing edges and consequent unphysical growth of TKE in the wake. The component $\max(c_{sep}\mu - \mu_T, 0)$ ensures that the separated flow source term is nullified once the transition has completed and prevents the wake from being corrupted by excessive turbulent production.

5 Model Calibration

5.1 The ERCOFTAC Flat Plate Test Cases

As mentioned in the Introduction section, for the calibration of the model, the flat plate experiments by the European Research Consortium on Flow, Turbulence and Combustion (ERCOFTAC) (Pironneau et al. 1992) were selected as test cases. The T3A, T3B, T3A-, and T3A-SK test cases are characterized by zero pressure gradient. The other test cases are instead characterized by a non-uniform freestream pressure distribution. Transition occurs in adverse pressure gradient conditions in T3C2, T3C3, T3C4. The last one is characterized by flow separation. Finally, T3C1 and T3C5 are characterized by transition in a favorable

Table 1 Boundary conditions and main flow variables for the T3 ERCOFTAC test cases

Test case	T3A	T3A-	T3A-SK	T3B	T3C1	T3C2	T3C3	T3C4	T3C5
$U_{in}[m/s]$	5.4	19.8	50.1	9.2	6.4	5.5	4.1	1.3	9.2
$Tu_{in}[\%]$	3.3	0.874	0.3	6.2	8.0	2.8	3.0	2.9	3.5
ν_T/ν	11.5	5.2	1.2	60.0	54.0	9.0	7.0	2.5	18.0

Table 2 Summary of the model constants

c_1	c_3	c_4	c_5	$c_{\mu,\ell}$	c_{sep}
0.02	0.02	8	24	0.03	10

pressure gradient. The boundary conditions and main flow quantities for the ERCOFTAC test cases are reported in Table 1.

The viscosity ratio (or turbulent Reynolds number) ν_T/ν was prescribed in order to match the experimental turbulence decay downstream of the plate leading edge. The same level of agreement documented in other works that employed the $k-\omega$ SST model (e.g. Menter et al. 2015) was obtained.

The computational domain was discretized using a single-block H-type mesh topology with 288 cells in the stream-wise direction and 128 in the wall-normal one. The plate leading edge was not included in the domain discretization and the flat lower boundary comprises 24 cells upstream of the plate and 264 on the solid surface. The mesh size was established on the basis of a grid independence analysis. The results of such an analysis will be discussed, as an example, only for the T3A- test case which indeed exhibits a very mesh sensitive transition behaviour. Free slip boundary conditions were imposed upstream of the flat plate leading edge and on the upper boundary. A uniform total pressure profile and parallel flow conditions were prescribed at the inlet of the computational domain. Uniform static pressure was assigned at the outlet.

The proposed values for the model constants are summarized in Table 2.

For all the ERCOFTAC test cases results obtained with the $\gamma - Re_{\theta,t}$ model are also reported for the sake of comparison.

5.1.1 Zero Pressure Gradient Cases

The constant c_1 controls LKE production (i.e. Eqs. 13 and 23), so it is believed that it has a major impact on the predicted transition path. As mentioned in Sect. 3, the constant c_5 acts as a transition onset parameter, so competing trends are to be expected if c_1 and c_5 constants are calibrated individually. The experimental profiles of fluctuation energy in the boundary layer are a valuable aid for establishing the proper values of such constants. Computed profiles of total fluctuation energy ($k_{tot} = k_\ell + k$) versus wall distance are compared to measurements in Fig. 2 for selected Re_x values in the transitional range and different couples of c_1 and c_5 constants. The values of c_1 and c_5 have been selected in order to fix the transition onset to the experimental location, as visible in Fig. 3a that reports the comparison between predicted and measured flat-plate skin-friction distributions. The c_1 value that ensures the best match with experiments is 0.02 and it corresponds to $c_5 = 24$, so these values are assumed as reference ones (Table 2).

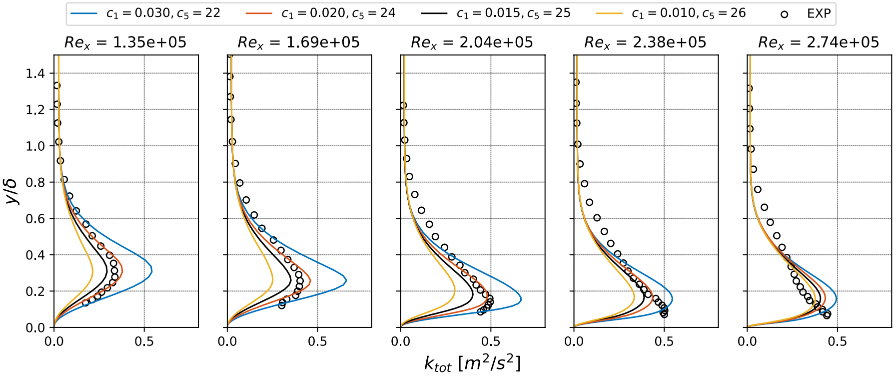

Fig. 2 Total fluctuation energy distributions versus wall distance for the T3A test case and different values of the c_1 and c_5 constants

The computed k_{tot} profiles agree well with measured ones up to $Re_x \simeq 2.0 \times 10^5$. In the last two locations reported in Fig. 2 ($Re_x = 2.38 \times 10^5, 2.74 \times 10^5$) the k_{tot} peak is predicted at a larger wall distance relative to the experimental one. A dominant contribution of the TKE is expected for such values of Re_x that correspond to the last stages of the transition process (see Fig. 3a). Thus it is expected that the turbulence model, rather than the transition modelling framework, plays a major role in determining the total fluctuation energy in the boundary layer in these locations.

It can be noticed how, in order to fix the transition onset location, the c_5 value must be decreased while increasing c_1. Such a behavior originates from the particular formulation of the intermittency factor: $k_{T,s}/(k_\ell + k_{T,s})$. A higher value of c_1 results in a higher level of k_ℓ and this tends to smooth the increase in intermittency. If not compensated with a decrease in c_5, such a mechanism causes an early onset and a delayed end of the transition process. This can also be inferred from Fig. 3a, where the c_f distribution obtained with the largest c_1 value ($c_1 = 0.03$, $c_5 = 22$) is the last one in reaching the fully turbulent level. Also in terms of skin friction distributions the best agreement with measurements is obtained with the proposed c_1, c_5 values.

The transition mechanism provided by the model for the T3A test case, for $c_1 = 0.02$ and $c_5 = 24$, is depicted in Fig. 3b that shows calculated distributions of LKE, TKE, transfer term R, and intermittency, as functions of the non-dimensional distance from the flat plate leading edge x/L (L flat plate length), taken at the wall distance where transition starts. The LKE increases monotonically up to approximately $x/L = 0.3$. This is the location where R comes into play promoting the transfer of energy from the laminar to the turbulent form, thus triggering transition. After the transition onset both the LKE and R rapidly decrease as expected, while the TKE increases. The intermittency starts to rise above zero at the transition onset and increases up to unity as a fully turbulent state is reached in the boundary layer.

For the constant c_4 the value used in the original model is retained. The constant c_3 controls the peak value of the transfer term R. A value of 0.02 guarantees the inception of turbulent production at the transition onset while providing a smooth increase in TKE up to the fully turbulent level. Values below 0.02 have been found to be too low

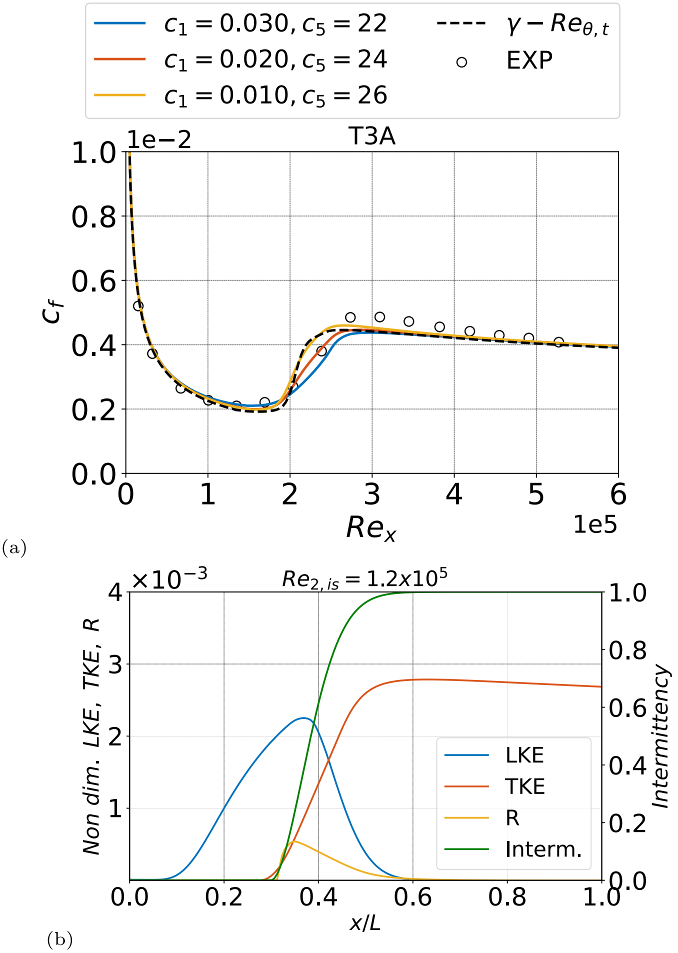

Fig. 3 **a** Skin friction distributions for the T3A test case, for different values of the c_1 and c_5 constants, and **b** distributions of transitional and turbulent quantities along the flat plate surface

to ensure a reliable transition start, while greater values only contribute to increase the peak in turbulent production that could result in a too rapid transition process.

The constant $c_{\mu,\ell}$ has a minor effect on the predicted transition path in zero and adverse pressure gradient boundary layers. On the contrary, it was found to have a non-negligible impact in favorable pressure gradient conditions, as will be discussed in subsection 5.1.2.

Figure 4 compares predicted and measured boundary-layer velocity profiles in the transition region for $c_1 = 0.02$ and $c_5 = 24$. The wall distance and local velocity are non-dimensionalized with the boundary layer thickness δ and the freestream velocity U_e respectively. Computed profiles appear in good agreement with experiments at all the considered locations.

In terms of skin-friction distributions, the current prediction for the T3A test case is compared with the one onbtained by coupling the LKE model with the Wilcox $k - \omega$ model in Fig. 5. The adopted model constants are the ones reported in Table 2 for both

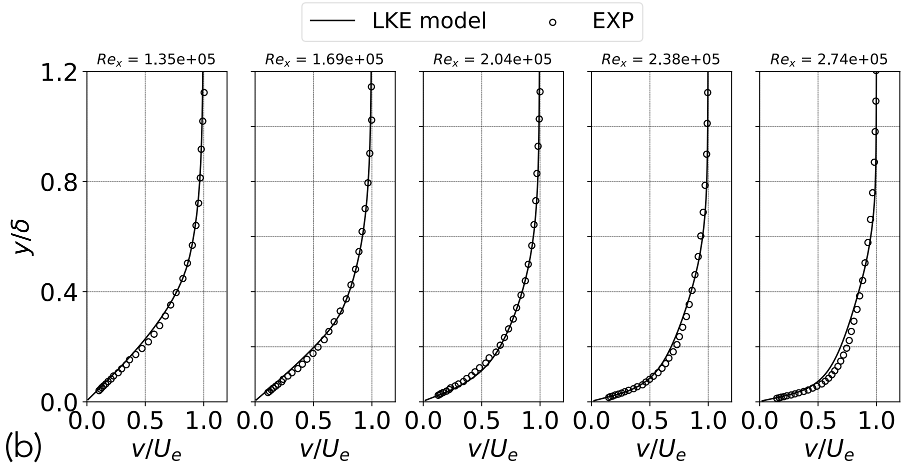

Fig. 4 Computed and measured boundary layer velocity profiles for the T3A test case

the calculations. The combined LKE+Wilcox $k-\omega$ transition/turbulence closure is seen to work properly, even if the comparison with the LKE+SST combination evidences a somewhat different behaviour. The transition onset is predicted at quite the same location, but the transition ramp and the fully turbulent level of c_f appear different. In particular, the transition process predicted with the Wilcox $k-\omega$ model appears to be quicker than the one provided by the SST model. This suggests that the model constants of Table 2 should be retouched depending on the particular model adopted as turbulence closure.

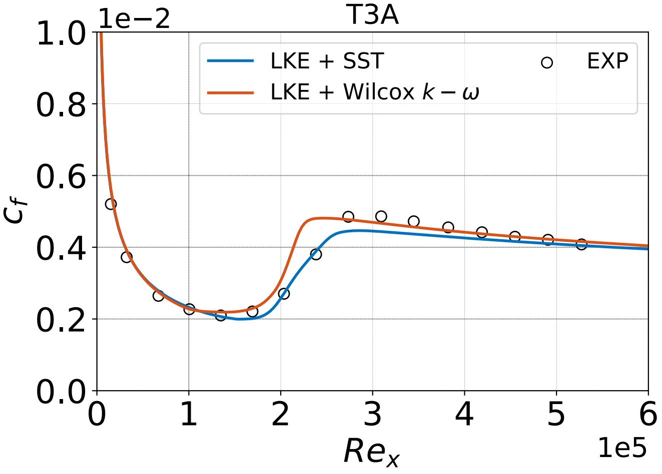

Fig. 5 Comparison between skin-friction distributions obtained with different turbulence models for the T3A test case

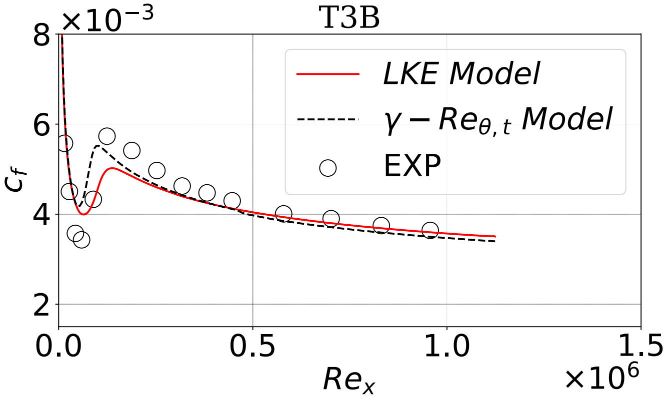

Fig. 6 Computed and measured skin-friction distributions for the T3B test case

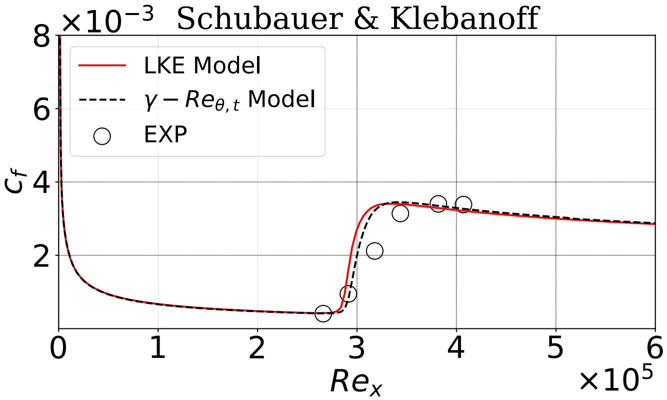

Fig. 7 Computed and measured skin-friction distributions for the Schubauer and Klebanoff test case

With the proposed set-up (Table 2), a good response by the model was recorded also for the higher freestream turbulence, higher Reynolds number T3B test case (Fig. 6). The transition onset location is correctly captured. However, discrepancies between calculated and measured skin friction distributions can be detected in the laminar portion of the boundary layer and in the peak at the end of transition. Neverthelesss, very few results in the open literature show better reproduction of those features (e.g. Walters and Cokljat 2008). The present predictions are probably affected by the approximate flat plate leading edge modelization mentioned in section 5.1.

Figures 7 and 8 report comparisons between measured and computed skin-friction distributions for the low freestream turbulence Schubauer-Klebanoff and T3A- flat plate test cases. Despite the fact that the proposed model has no specific component for natural transition, it was considered interesting to check for its capabilities in such flow configurations too. As mentioned, for the T3A- test case (Fig. 8), skin friction distributions are reported for all the three mesh sizes used for the grid independency analysis on the ERCOFTAC flat plate test cases. The grid dimensions are reported in Table 3. Only the coarse grid calculation seems off in terms of predicted transition onset location relative to the other two

Table 3 Mesh dimensions for grid dependency analysis

Coarse	Medium	Fine
165×65	289×129	541×221

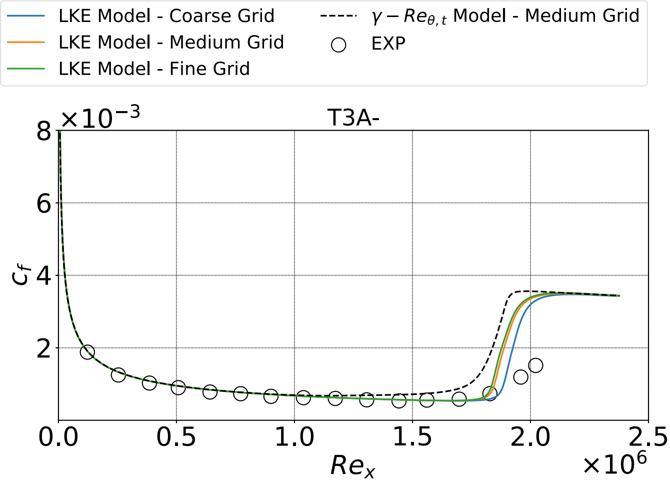

Fig. 8 Measured and computed skin-friction distributions for three different mesh sizes for T3A- test case

grids and measurements. The medium and fine grids yield essentially the same results so that space convergence was assumed as reached on the medium grid. The transition path is definitely too steep in all the calculations, including also the $\gamma - Re_{\theta,t}$ model result. This is true also for the Schubauer-Klebanoff test case with reference to both LKE and $\gamma - Re_{\theta,t}$ calculations. However, the present predictions of T3A- and Schubauer-Klebanoff flow configurations appear in line with the ones reported in other works (e.g. Menter et al. 2015).

5.1.2 Favorable Pressure Gradient Cases

Measured and calculated skin-friction distributions for the T3C1 test case are compared in Fig. 9. Although the transition onset location seems to be captured correctly, there is a significant misrepresentation of the laminar boundary layer prior to transition, with a relevant overestimation of c_f. Like for the T3B test case, transition starts shortly downstream of the leading edge, and again the simplified modelization of this geometrical feature is deemed to be responsible for the observed discrepancies. Although this test case is seldom presented in the literature, like in Menter et al. (2006, 2015), some results by other researchers appear similar to the present prediction (e.g. Li et al. 2021).

As mentioned in Sect. 4.3, the $c_{\mu,\ell}$ constant, which controls the amount of laminar fluctuations eddy viscosity introduced in the diffusive terms of the governing equations, is found to have a non-negligible impact on the transition path in favorable pressure gradient conditions.

A sensitivity analysis to the $c_{\mu,\ell}$ value is presented, in terms of skin-friction distributions in Fig. 10a, and in terms of boundary layer velocity profiles in Fig. 10b. The

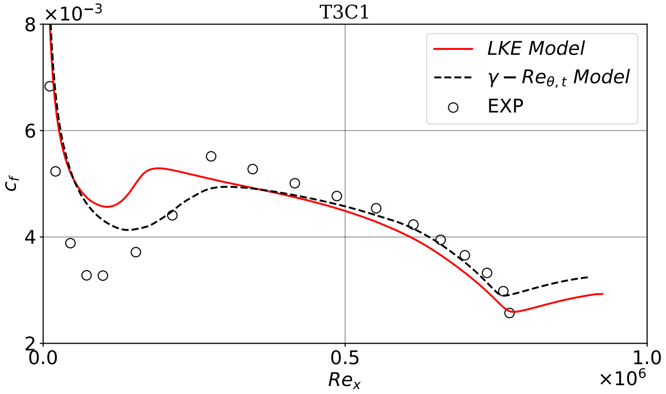

Fig. 9 Computed and measured skin-friction distributions for the T3C1 test case

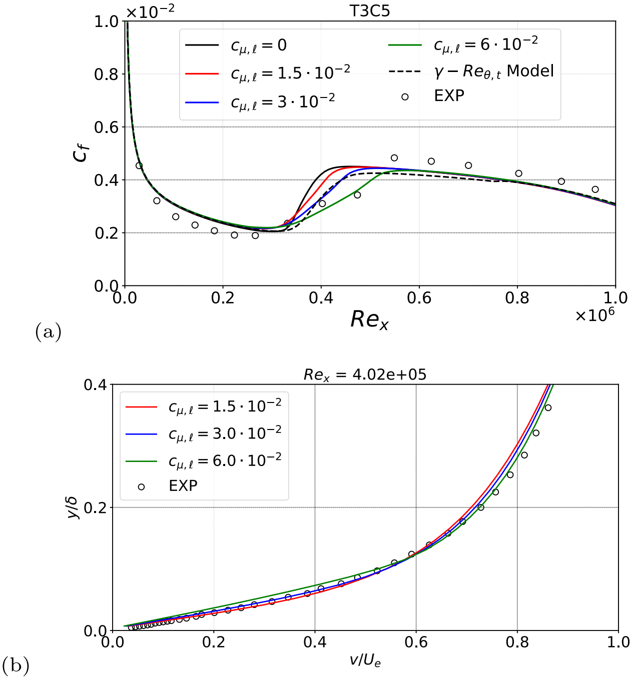

(a)

(b)

Fig. 10 Computed and measured skin-friction distributions (**a**), and boundary layer velocity profiles for the T3C5 test case for different values of the constant $c_{\mu,\ell}$

$c_{\mu,\ell}$ value does not influence the transition onset, but it shows a noticeable effect on the transitional c_f ramp (Fig. 10a). Increasing $c_{\mu,\ell}$ results in a smoother transition path that tends to widen the transition region and delay the attainment of the fully turbulent regime. The best agreement with experimental data is achieved with $c_{\mu,\ell} = 0.03$, so this is proposed as the constant standard value (see Table 2). The analysis of boundary layer velocity profiles taken midway through the transition process ($Re_x = 4.02 \times 10^5$), and reported in Fig. 10b, further justifies such a choice. In fact, the velocity profile predicted with $c_{\mu,\ell} = 0.03$ shows the best overall agreement with measurements. Interestingly, the $\gamma - Re_{\theta,t}$ prediction agrees very well with the one by the LKE model with $c_{\mu,\ell} = 0.03$.

5.1.3 Adverse pressure gradient cases

First attempts for assessing the model performance against the adverse pressure gradient test cases T3C2, T3C3, and T3C4 consistently resulted in a significant delay in the prediction of the transition onset location relative to experimental data. This is evident from the results of Fig. 11, where the skin-friction distribution calculated with the proposed value for the constant c_5 clearly exhibits the effect of a retarded transition. Such a behaviour of the model suggests that, c_5 should be sensitized to positive pressure gradients. Actually, for sake of generality, also a dependence from the freestream turbulence level should be introduced in the transition parameter formulation, even if the pressure gradient seems to have a leading role in determining the correct c_5 value. These observations identify thec_5 parameter as a good candidate for data-driven modifications via machine-learning approaches. Here, as a proof of concept, simple linear expressions as a function of pressure gradient parameters are proposed.

The first one is based on the f_{PG} parameter defined by equation 22:

$$c_5(f_{PG}) = \begin{cases} 24 & f_{PG} \leq 0 \\ 24 - 2f_{PG} & f_{PG} > 0 \end{cases} \tag{28}$$

and the second one is based on $\lambda'_{\theta L} = -[\nabla(\mathbf{U} \cdot \mathbf{n}) \cdot \mathbf{n}]\frac{y^2}{\nu}$, the Menter's parameter without the constants reported in equation 21:

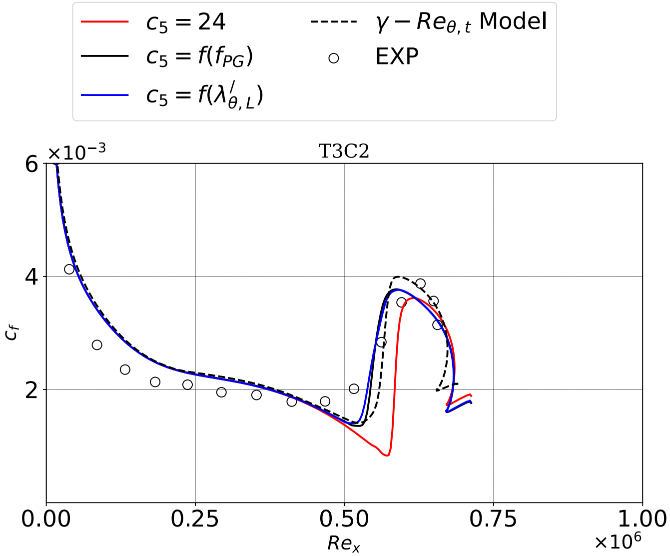

Fig. 11 Skin-friction distributions for the T3C2 test case obtained with different formulations for c_5

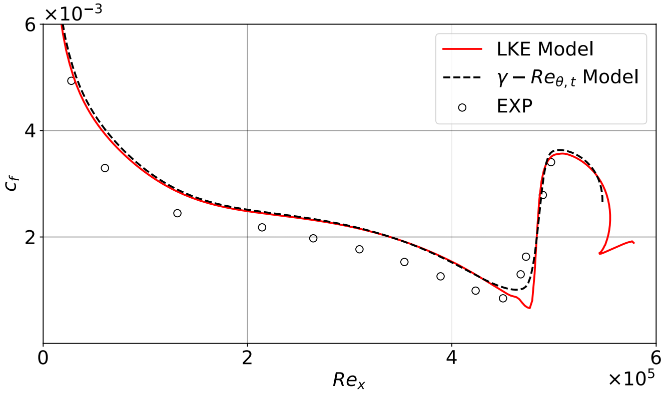

Fig. 12 Computed and measured skin-friction distributions for the T3C3 test case

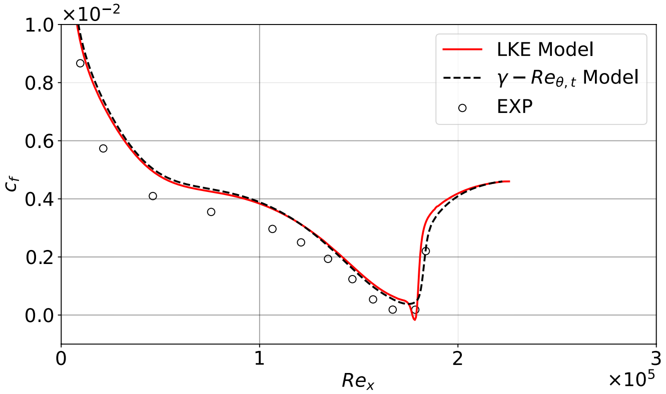

Fig. 13 Skin-friction distributions for the T3C4 test case with different transition models

$$c_5(\lambda'_{\theta L}) = \begin{cases} 24 & \lambda'_{\theta L} \geq 0 \\ 24 + 5.5\lambda'_{\theta L} & \lambda'_{\theta L} < 0 \end{cases} \tag{29}$$

The improvement in the predictions for the T3C2 test case can be clearly appreciated in Fig. 11, with almost coincident results by Eqs. 28 and 29. The proposed functional forms for c_5 yield good predictions also for the T3C3 and T3C4 test cases, as witnessed by Figs. 12 and 13, where measured skin-friction distributions are compared with numerical results obtained with Eq. 28. However, it is worth noticing how the predicted transition region is consistently too short relative to experimental data. Despite a small separation is detected in the computed T3C4 flow configuration, it is noted how the separation-specific model component (Eq. 24) does not activate. This is due to transition being triggered by the c_5 modification according to Eq. 28 prior to the activation of the f_{sep} function (Eq. 26) in this case.

Table 4 Main flow conditions for the VKI-LS89 vane cascade

Test case	$M_{2,is}$	$Re_{2,is}$	$Tu[\%]$	ℓ_t/C_x
Mur224	0.927	5.919×10^5	6.0	0.08
Mur228	0.932	5.955×10^5	1.0	0.04
Mur239	0.927	2.14×10^6	6.0	0.04
Mur247	0.922	2.117×10^6	1.0	0.014

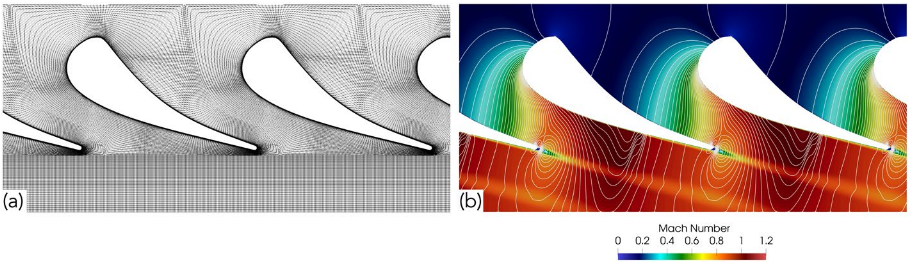

Fig. 14 Multiblock O–H grid for the LS89 cascade (every second line shown) (**a**), and pressure isolines superimposed to color Mach number contours for the Mur239 test case (**b**)

6 Model Validation

All the calculations that will be reported have been carried out with the complete formulation of the model, starting from what presented in Sect. 4, and including the corrections for pressure gradient (Eq. 28), separated flow (Eq. 24), and the laminar diffusivity (Eq. 19). This latter term is added to the eddy viscosity in the diffusive fluxes of the Navier–Stokes equations.

6.1 Bypass transition in the VKI-LS89 cascade

This section discusses computed results for the VKI-LS89 test case (1990), which is based on a linear cascade representative of high-pressure turbine stator vane. It was tested experimentally at the von Kármán Institute for Fluid Dynamics (VKI) in the framework of a comprehensive aerothermal investigation campaign. External heat transfer measurements were acquired in subsonic as well as transonic flow conditions for a variety of Reynolds numbers and inlet freestream turbulence values. The heat transfer coefficient distribution is extremely effective in highlighting the boundary layer transition path and for such a reason this was considered as an interesting test case for validating the proposed transition model. The blade boundary layers undergo bypass transition in the majority of the experimentally tested flow configuration. The main flow conditions for the test cases presented in this work are summarized in Table 4.

The cascade flow domain was discretized using an O-H grid with 858 mesh points on the blade surface, and 256 in the pitch-wise direction for a total of about 300K cells. A view of the computational grid is reported in Fig. 14a. Transonic flow conditions were detected for all the considered test cases, as evident from Fig. 14(a), which reports static pressure isolines superimposed to color Mach number contours for the Mur224 configuration. The Mach number reaches a value of about 1.1 downstream of the cascade throat, which results in a normal shock wave located approximately midway between the throat section and the blade trailing edge.

Figure 15a, and b report the comparison between computed and measured blade surface heat transfer coefficient H distributions for two different exit isentropic Reynolds number values ($Re_{2,is} = \rho_{2,is} v_{2,is} C_x / \mu_{2,is}$, where C_x is the blade axial chord and the subscript 2 denotes outlet flow conditions). In such figures, H is reported as a function of the non-dimensional curvilinear abscissa (s/s_{tot}) along the blade surface. Negative values refer to the blade pressure side while positive ones are taken on the suction side. The origin is placed on the leading edge. For each Reynolds number value, results for the highest and the lowest experimentally tested turbulence intensities ($Tu = 6\%$ and $Tu = 1\%$) are compared with predictions.

No information about the turbulent length scale for the various test cases was given in the original report (Arts et al. 1990), so as a criterion for establishing the correct turbulence decay, it was decided to set its value in order to match the heat transfer coefficient level at the blade leading edge for each case, as visible in Fig. 15a, and b. With the $k-\omega$ SST model, this resulted in the non-dimensional turbulent length scale (ℓ_T/C_x) values reported in Table 4. First attempts to exploit such a data matching strategy with the Wilcox $k-\omega$ model resulted in leading-edge heat transfer coefficients always remaining below the measured level, even when exaggerating the turbulent length scale value. This is suspected to be related to the realizability constraint (Durbin 1996), the adoption of which was found to be mandatory for obtaining physically consistent results with the Wilcox $k-\omega$ model.

The numerical results for the flow configurations at the lowest Reynolds number (Mur224 and Mur228, $Re_{2,is} \simeq 6 \times 10^5$) can be assessed on the base of Fig. 15a. On the blade suction side, the transition onset location is reasonably well predicted for both low and high inlet freestream turbulence conditions.

On the blade pressure side, no clear indication of transition can be inferred from the experimental data and calculations also predict laminar flow up to the trailing edge. Pressure side measurements only show different heat transfer coefficient levels for the two test

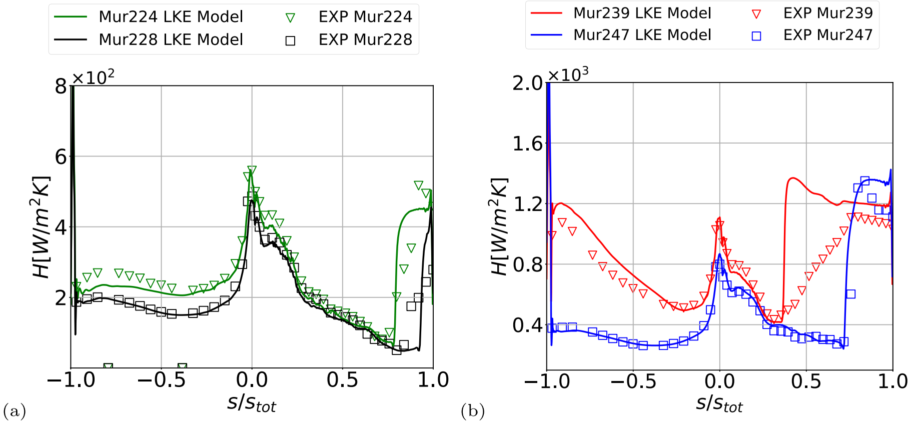

Fig. 15 Heat transfer coefficients distributions for (**a**) Mur224-Mur228, and (**b**) for the Mur239-Mur247 test cases

cases that are deemed to be the result of the freestream turbulence perturbing the laminar boundary layer. Such an effect is reasonably reproduced by the current framework. For the cases at higher Reynolds number corresponding to $Re_{2,is} \simeq 2 \times 10^6$ (Mur239 and Mur247, Fig. 15a, the transition onset locations predicted by the proposed model on the blade suction side are in very good agreement with the experimental ones. In the calculation at higher freestream turbulence (Mur239) transition occurs on the pressure side too, with an onset location predicted at approximately $s/s_{tot} = 0.4$ and the computed heat transfer coefficient distribution is in very good agreement with the experimental one.

More insights on the transition process provided by the LKE model on the VKI-LS89 cascade can be deduced from Fig. 16 that shows distributions of LKE, TKE, transfer term and intermittency as a function of the non-dimensional axial coordinate on the blade suction side for the Mur239 (Fig. 16a), and Mur247 (Fig. 16b) test cases. The schockwave impinges the suction side at $x/C_x = 0.83$ and forces transition to occur at this same location only for the low freestream turbulence flow configuration (Mur247, Fig. 16b). For the highest freestream turbulence flow case ((Mur239, Fig. 16a) transition actually occurs ahead of the shock. The depicted mechanism is similar to the one discussed for the ERCOFTAC T3A test case, with the LKE gradually increasing up to the transition onset, which appears to be driven by the transfer term R, which forces the inception of TKE production that later follows the increase in intermittency. In all the calculations of the VKI-LS89 cascade transition is seen to develop too quickly relative to what happens in the measurements. This is evident from the computed results of Figs. 15a, and b, especially for the Mur239 test case, where experiments show a very smooth increase in the H distribution after the transition has started. However, this aspect of the present results appears consistent with what is observed in the majority of RANS analyses reported in the literature for this cascade (e.g. Walters and Cokljat 2008, Menter et al. 2006). More realistic distributions of the heat transfer coefficient associated with the prediction of a smoother transition process, more in line with experimental results, have been obtained with quasi-DNS calculations by Segui et al. (2017).

6.2 Separated-Flow Transition in High-Lift Low Pressure Turbine Cascades

As mentioned in the introduction section, two test cases, based on different high-lift cascades operating in low-pressure-turbine-like conditions, were selected to check for

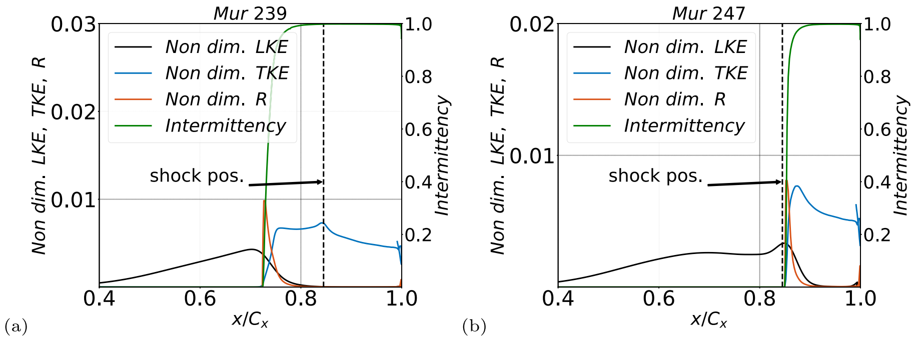

Fig. 16 Distributions of transitional and turbulent quantities along blade suction surface for (**a**) Mur239 and (**b**) Mur247 test cases

Table 5 Main flow parameters for the T106C and T108 cascades (α_1 and α_2 are the inlet and outlet blade angles)

Test case	α_1	α_2	*pitch/chord*	$M_{2,is}$
T106C	32.7^o	65^o	0.95	0.6
T108	35.5^o	65^o	1.1	0.6

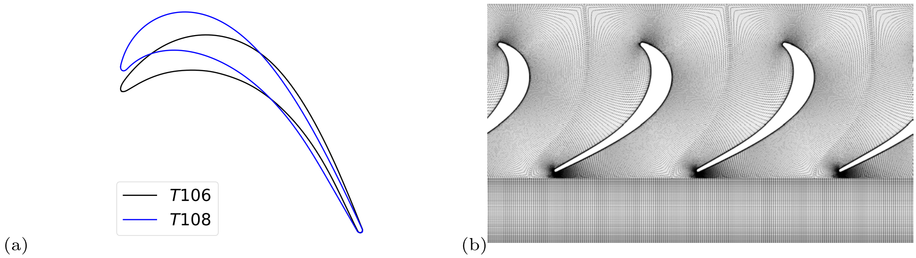

Fig. 17 **a** Cascades geometries and, **b** O–H multi-block grid for the T108 cascade (every second line shown)

the capability of the proposed model to deal with separated-flow transition in turbomachinery-relevant flow configurations. The two cascades are built on the T106C and T108 blade sections (Fig. 17a). They share the same inlet and exit Mach numbers, and approximately the same deflection, but the T106C is characterized by an aft-loaded profile, while the T108 is front-loaded, and this results in a much gradual diffusion from the suction velocity peak up to the blade trailing-edge. Flow topologies are then expected to be sensibly different in terms of separation point locations and bubble sizes. The main geometric and flow conditions for the two test cases are summarized in Table 5.

A multi-block O–H type grid structure was adopted for discretizing the computational domain of the two cascades, with 660 mesh points on the blade surface, and 140 in the pitch-wise direction. The H-type block stitched to the outlet boundaries of the O mesh, is characterized by almost uniform mesh spacing in the axial and tangential directions in order to allow optimal resolution in the wake region. A view of the computational grid for the T108 cascade is reported in Fig. 17b.

The T106C and the T108 cascades were experimentally tested at the von Kármán Institute in the framework of the European research projects UTAT and TATMo (see also Michálek et al. 2012, Pacciani et al. 2014). Experimental results are available for several exit isentropic Reynolds number values, ranging from 0.8×10^5 to 1.6×10^5. The flow configurations considered in this work are the ones characterized by the lowest freestream turbulence value ($Tu = 0.8\%$). In such conditions, the transition occurs on the blade suction side due to separated flow for all the tested Reynolds numbers, while the pressure side boundary layer remains entirely laminar. For the T106C cascade, when lowering the Reynolds number the suction side flow structure experiences the transition from short to long bubble configurations and even open separations, a mechanism generally known as *bubble bursting* (Gaster 1969; Lou and Hourmouziadis 2000). The inlet turbulent length scale was selected by matching the experimental

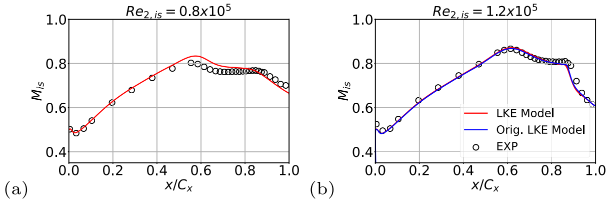

Fig. 18 Isentropic Mach number distributions for the T106C cascade: **a** $Re_{2,is} = 0.8 \times 10^5$, **b** $Re_{2,is} = 1.2 \times 10^5$, and **c** $Re_{2,is} = 1.6 \times 10^5$

turbulence decay upstream of the cascade leading edge and corresponds to the value of $\ell_T/C_x = 2.5 \times 10^{-3}$, as a fraction of the blade axial chord.

All the numerical predictions discussed in this section of the paper have been obtained from converged, in terms of residual decrease, steady calculations. Figure 18 compares computed and measured blade suction surface isentropic Mach number distributions, while Fig. 19 reports wake loss profiles for the T106C cascades at three different exit isentropic Reynolds number values. In Fig. 19 the tangential coordinate y is non dimensionalized with the cascade tangential pitch g and the total pressure loss coefficient is defined as: $Y = (p_{01} - p_{02})/p_{01}$. The positive y axis direction is from the suction side of one blade to the pressure side of the adjacent one. The loss coefficient distributions have been moved tangentially in order to have the calculated peak location coincident with the experimental one. This facilitates the comparison in terms of loss peak and wake width. The inlet total pressure p_{01} is acquired just upstream of the blade leading edge, while the pitch-wise distribution of outlet total pressure p_{02} is obtained by traversing the wake at 46.5% axial chord downstream of the trailing edge. In agreement with the experimental data reduction, p_{01} and p_{02} are mass averaged quantities.

At the lowest Reynolds number value ($Re_{2,is} = 0.8 \times 10^5$, Figs. 18a, and 19a) the isentropic Mach number distribution along the blade suction side shows the effects of an open separation rather than a closed bubble. This is witnessed by a M_{is} value at the trailing edge that is higher than the outlet value. Indeed, the numerical results predict an open separation for such flow conditions, but the experimental isentropic Mach number distribution is not perfectly reproduced by the calculation (Fig. 18a). The computed distribution suggests that transition is predicted too early and this results in a smaller extent of the separated flow region. This reflects of the wake loss profile prediction at this

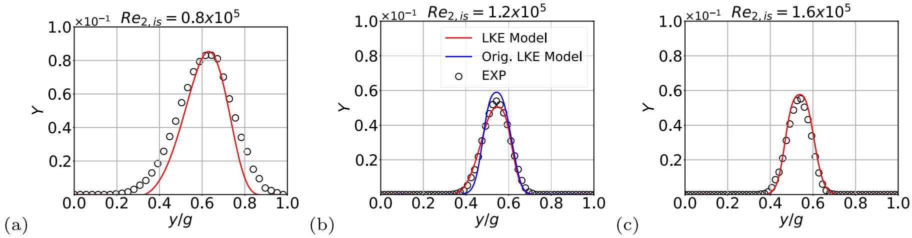

Fig. 19 Pitch-wise distributions of total pressure loss coefficient for the T106C cascade: (a) $Re_{2,is} = 0.8 \times 10^5$, (b) $Re_{2,is} = 1.2 \times 10^5$, and (c) $Re_{2,is} = 1.6 \times 10^5$

Reynolds number value (Fig. 19a). In fact, the measured wake width appears wider than the computed one. A larger separation results in a thicker turbulent boundary layer after transition and reattachment, and this contributes to a more intense wake mixing. This justifies the discrepancies between computed and measured wake loss profiles observed in Fig. 19a. With the aid of full-span LES calculations, Rosenzweig et al. (2023) have shown how three-dimensional effects related to secondary-flow-driven boundary layer migration play a key role in determining the separation and wake structures at mid-span for this Reynolds number value. So, The numerical results of Figs. 18a, and 19a are considered satisfactory for a purely two-dimensional RANS approach. For higher Reynolds number values the suction side isentropic Mach number distributions suggest that the flow topology is characterized by laminar separation bubbles, with boundary layer reattachment after transition, and computed results are in better agreement with experiments Figs. 18b, c), and 19(b, c). The surface isentropic Mach number appears slightly underestimated in the separation bubble region and this could suggest that the experimental separation bubble is thicker than the computed one. However, it is worth noting how the proposed framework shows remarkable capabilities for predicting the profound modifications occurring, for the T106C cascade, in the separation structure and blade loading when varying the Reynolds number. On the entire Reynolds number range, the predictions by the present model appear in harmony with the ones obtained with the original LKE model (e.g. Pacciani et al. 2014). The results by the two approaches are compared in Figs. 18b, and 19b, for $Re_{2,is} = 1.2 \times 10^5$, as an example. The suction side isentropic Mach number distributions are practically coincident, while the revised LKE model results in a slightly better wake loss profile prediction both in terms of peak value and pitchwise width.

The comparison between computed and measured integrated loss coefficients as a function of the exit isentropic Reynolds number (i.e. the cascade lapse rate), depicted in Fig. 20(b), is in line with what is discussed for Fig. 19 in terms of wake loss profiles. The integral loss is underestimated at the lowest Reynolds number and reasonably well predicted for the higher Reynolds numbers.

In order to highlight the role of the separation-related components of the proposed framework, suction surface distributions of relevant transitional/turbulent quantities are shown in Fig. 20b for the intermediate Reynolds number value ($Re_{2,is} = 1.2 \times 10^5$). The reported distributions are taken at a distance from the wall where transition occurs. The

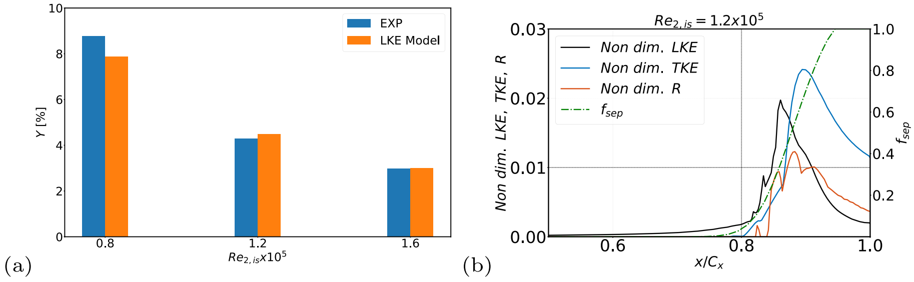

(a) (b)

Fig. 20 (a) Distributions of transition and turbulent models quantities along the blade suction side for $Re_{2,is} = 1.2 \times 10^5$, and (b) integrated loss as a function of $Re_{2,is}$ for the T106C cascade

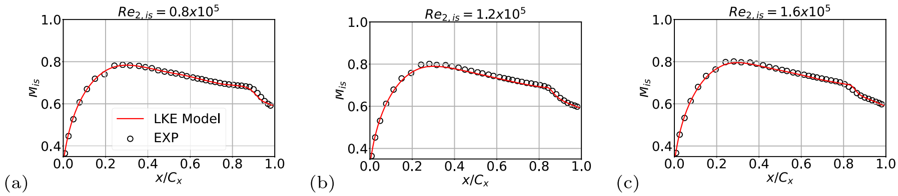

Fig. 21 Isentropic Mach number distributions for the T108 cascade: **a** $Re_{2,is} = 0.8 \times 10^5$, **b** $Re_{2,is} = 1.2 \times 10^5$, and **c** $Re_{2,is} = 1.6 \times 10^5$

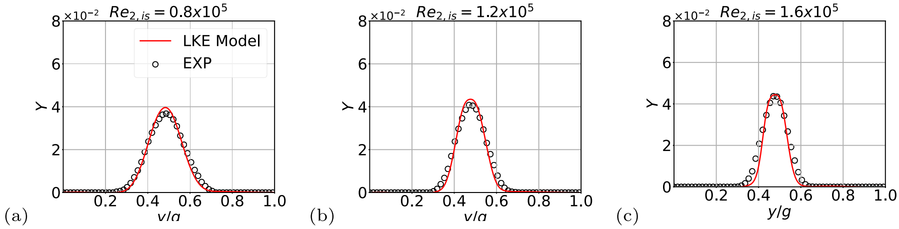

Fig. 22 Pitch-wise distributions of total pressure loss coefficient for the T108 cascade: **a** $Re_{2,is} = 0.8 \times 10^5$, **b** $Re_{2,is} = 1.2 \times 10^5$, and **c** $Re_{2,is} = 1.6 \times 10^5$

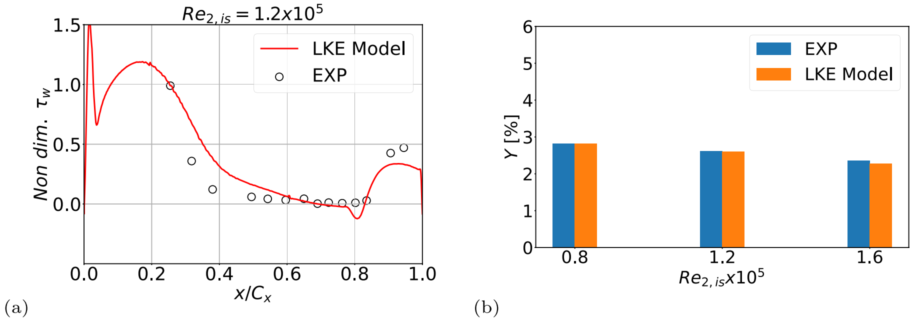

Fig. 23 **a** Skin-friction distribution along the blade suction side for $Re_{2,is} = 1.2 \times 10^5$, and **b** integrated losses for the T108 cascade

f_{sep} function becomes greater than the zero at approximately 80% of the blade axial chord, where the separation point is located, and rapidly increases downstream driving the growth of the LKE in the separated shear layer. This mechanism can be inferred from the kink in the LKE distribution near the separation point location. The contribution of f_{sep} in boosting the transfer term R at transition can also be appreciated in Fig. 20b.

The numerical results for the T108 cascade are compared with measurements in Fig. 21 (suction surface isentropic Mach number distributions) and Fig. 22 (wake loss profiles). As for the 106C cascade, wake traverses are taken at $0.465C_x$ downstream of the blade trailing edge. For all the considered Reynolds numbers the suction side laminar separation has the structure of a short bubble. Also for this test case, the computed results well capture the separation bubble evolution when varying the Reynolds number and nicely match the experimental data for all the considered flow conditions.

Figure 23a shows the comparison between suction side distributions of computed wall shear stress and experimental quasi-wall shear stress for the intermediate Reynolds number value ($Re_{2,is} = 1.2 \times 10^5$). For such a comparison to make sense, all the datasets must be consistently non-dimensionalized with a reference value. The τ_w value corresponding to the location of the first measurement on the blade suction side was chosen for such a scaling. With no doubt about the only qualitative nature of the comparison, it is observed how the computed separated flow region almost perfectly covers the blade suction side fraction characterized by zero quasi wall shear stress, with well-captured separation and reattachment locations. The experimental distribution shows a higher level of τ_w after reattachment relative to the numerical results. This is deemed to be due to the turbulence model rather than to the transition modelling framework.

Consistently with the general good agreement between measurements and calculation, the cascade lapse rate is also well predicted as visible in Fig. 23b.

The model performance appeared to be quite insensitive to the constant c_{sep} value. It was varied in the range $10 - 100$ without observing significant changes in the computed results. Values higher than 100 tend to results in a too steep pressure recovery after reattachment, while for values lower than 10 the onset of instabilities can sometimes be detected in the separated shear layer, leading to unsteady transition paths. A value of 10 was considered satisfactory (see Table 2). For a more precise and physically consistent calibration of c_{sep} detailed experimental or high-fidelity studies of the instabilities developing in the separated shear-layer would be desirable.

6.3 Transition Under Low Freestream Turbulence Conditions on the S809 Airfoil

The S809 airfoil was calculated, in incompressible flow conditions, for a Reynolds number value of 2×10^6. Following the studies of other researchers (e.g. Walters and Cokljat 2008), the inlet freestream turbulence intensity was set to 0.2% and a value of 10 for the

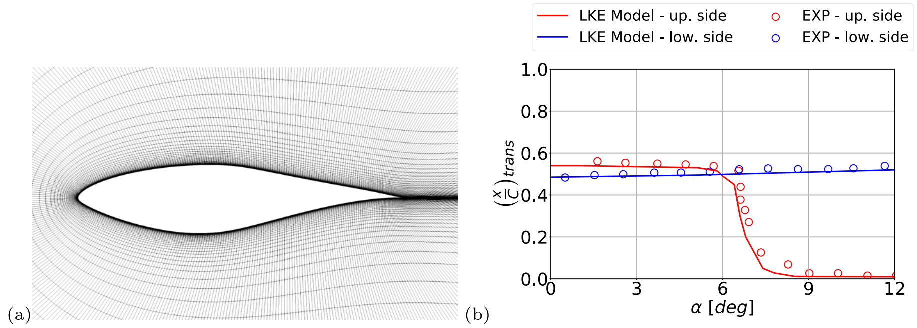

Fig. 24 **a** 720x180 C-type grid (every second line shown), and **b** transition onset location as a function of the angle of attack for the S809 airfoil

viscosity ratio was assumed. A single-block C-type grid topology was used to discretize the computational domains that extends 40 chords away from the airfoil surface. A number of 720 cells were distributed on the solid surface and the wake centerline (coincident with the mesh branch-cut), while 180 cells were used in the normal-to-the-wall direction. An enlarged view of the computational grid in the vicinity of the airfoil is shown in Fig. 24a.

Measured transition locations on both the airfoil sides are available for a range of angles of attack, and such a dataset provides a very good opportunity to test the predictive capabilities of a transition model. In order to study the evolution of the transition process when varying the incidence, the range between 0^o and 12^o in terms of angle of attack (α) values was spanned with 20 calculations. Such calculations include the experimentally tested incidence values. The predicted non-dimensional chord-wise positions of the transition onset locations are compared to experiments in Fig. 24b. For α ranging from 0^o up to approximately 5.5^o transition is predicted to occur due to separated flow on both the upper and the lower side of the airfoil. In order to support this observation, the airfoil surface distribution of non-dimensional wall shear stress for $\alpha = 0^o$ is reported, as an example, in Fig. 25a. Here negative values of the non-dimensional chord-wise coordinate x/C refer to the airfoil's lower side, while positive values refer to the upper one. For this angle of attack, the mild boundary-layer separation occurring on the airfoil upper side can also be inferred from the pressure coefficient distributions of Fig. 25b. In fact, both computed and measured C_p distributions show, on the airfoil upper side, a small pressure plateau, at approximately $x/C = 0.5$. The pressure coefficient is defined as: $C_p = \frac{(p_{0,\infty}-p)}{\rho U_\infty^2/2}$, with $p_{0,\infty}$ and U_∞ freestream total pressure and flow velocity. Predictions agree well with experiments, and the same level of agreement was recorded for all the experimentally tested incidence values. On the airfoil suction side, the transition onset location rapidly moves upstream for $\alpha > 5^o$, and consistently sits in the vicinity of the leading edge for $\alpha > 9^o$. This behaviour is quite correctly reproduced by the calculations, even if transition is predicted to occur slightly upstream relative to measurements at all the considered angles of attack. Such a discrepancy can be noticed on the airfoil pressure side too, but again the smooth trend in the transition onset location drift towards the trailing edge is correctly captured in the numerical predictions.

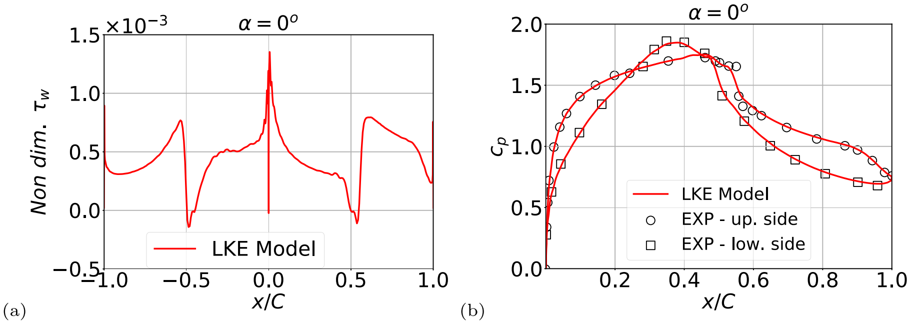

(a) (b)

Fig. 25 **a** wall-shear stress, and **b** pressure coefficient distributions at zero angle of attack for the S809 airfoil

7 Conclusion

A novel LKE-based transition modelling framework is proposed. A previous formulation, specifically developed for separated-flow transition, has been extended towards the prediction of bypass transition too. The work is aimed at constructing a framework suitable for further data-driven improvements using machine learning approaches. The LKE production and transfer terms have been selected for model modifications, and new formulations have been introduced to mimic the growth of pre-transitional fluctuations in boundary layers and separated shear layers under the effect of variable pressure gradients and freestream turbulence. A reliable coupling of the LKE transport equation with two-equation turbulence model has been achieved by providing the framework with a suitably devised intermittency factor. Although the model is more of a base framework for data-driven enhancements, some simplified closure functions are provided as proof of concept. Unlike other LKE-based models, not only phenomenological arguments have been adopted for the definition of the closure functions, but ideas and formulations of local non-dimensional terms have been also borrowed from local correlation approaches. This enhances the generality and flexibility of the model facilitating in the perspective of a data-driven training of those functions. The proposed model makes use of local quantities only, but it is not Galilean invariant. The calibration of the constants and functions has been made with reference to the ERCOFTAC flat plate test cases. Detailed analyses of the zero pressure gradient case has allowed a tuning of the LKE production term that ensures a realistic growth of the fluctuation energy in the transition region. The introduction of a pre-transitional fluctuation diffusivity was found to improve predictions in favorable pressure gradients. Transition in adverse pressure gradient was addressed by relying on local indicators like in local correlation-based models. Specific terms were added to address the growth of instabilities in separated shear layers and their subsequent breakdown to turbulence, thus allowing separated-flow transition predictions. The validation campaign was carried out, mostly on turbine cascades, over a wide range of flow conditions. The model shows a realistic response to freestream turbulence and Reynolds number and, overall, the comparison with experimental data shows a level of accuracy in predicting the transition onset that appears in line with engineering requirements. Separated-flow transition predictions show essentially the same accuracy of the baseline model that was specifically conceived for such a purpose. However, some questions regarding the calibration of the separated-flow transition term remains open and need further insights in the development of instabilities in the separated shear-layer to be answered. This issue could be addressed in the future with the aid of detailed experimental or high-fidelity results.

Despite the model does not include a specific component for natural transition, its performance in predicting transition in low freestream turbulent conditions was found to be promising on flat plate cases and airfoils. However, predicted transition regions appear consistently too short relative to measurements, and this clearly highlights the scope for improvement in the predicting capabilities of the model. Finally, It is believed that the proposed model is flexible and general enough to serve as a suitable basis for data-driven training with machine learning approaches.

Appendix A Model Formulation

The model is based on the following three transport equations:

$$\frac{Dk_\ell}{Dt} = \tilde{P}_\ell - R - D_\ell + \frac{\partial}{\partial x_j}\left(\nu \frac{\partial k_\ell}{\partial x_j}\right) \tag{A1}$$

$$\frac{Dk}{Dt} = P_k + R - D_k + \frac{\partial}{\partial x_j}\left[\left(\nu + \frac{\nu_T}{\sigma_k}\right)\frac{\partial k}{\partial x_j}\right] \tag{A2}$$

$$\frac{D\omega}{Dt} = P_\omega - D_\omega + \frac{\partial}{\partial x_j}\left[\left(\nu + \frac{\nu_T}{\sigma_\omega}\right)\frac{\partial \omega}{\partial x_j}\right] + CD_{k\omega} \tag{A3}$$

The LKE production term $\tilde{P}_\ell$ is given as:

$$\tilde{P}_\ell = (1-\gamma)P_\ell, \quad P_\ell = c_1\left(\frac{\Omega y^2}{U}\right)S^2\sqrt{k_{T,l}} + f_{sep}P_{sep} \tag{A4}$$

where:

$$k_{T,l} = k - k_{T,s}, \quad k_{T,s} = f_{SS}k, \quad f_{SS} = e^{-\left(\frac{c_{SS}\nu\Omega}{k}\right)^2}, \tag{A5}$$

$$f_{sep} = 1 - e^{\left[-\max\left(\frac{Re_\nu}{R_{cr}}-1,0\right)\right]}, P_{sep} = \max(c_{sep}\mu - \mu_T, 0)S^2, \tag{A6}$$

$$R_{cr} = 800\max\left[\min(2r,8),1\right], r = \frac{Sy}{U}, Re_\nu = \frac{Sy^2}{\nu}. \tag{A7}$$

The LKE destruction term D_ℓ is:

$$D_\ell = 2\nu\frac{k_\ell}{y^2} \tag{A8}$$

The transfer term R is as follows:

$$R = c_3(f_t + 3c_{sep}f_{sep})k_\ell\omega \tag{A9}$$

with:

$$f_t = \left(1 - e^{-\frac{\psi}{c_4}}\right), \quad \psi = \max\left(\frac{\sqrt{k}y}{\nu} - c_5, 0\right), \tag{A10}$$

The f_{sep} term is a separation-aware term that is used to activate the model's components for separated-flow transition. The current form of such a term is reported in Eq. 26, where it is expressed as a function of the ratio between an indicator, the vorticity Reynolds number Re_ν, and a critical term. The critical term, in general, should be a function of the pressure gradient and a local parameter quantifying the turbulence coming from the freestream. The c_5 term is a threshold quantity that acts as a transition parameter. It should also be a function of the pressure gradient and freestream turbulence. Proposals that only account for the pressure gradient are reported in Eqs. 28 and 29. The turbulence equations are the ones of the $k-\omega$ SST model (Menter 1994), with:

$$\tilde{P}_k = \gamma P_k, \quad \tilde{D}_k = \max(\gamma, 0.1) D_k \tag{A11}$$

The intermittency factor γ is given by (see equation 14):

$$\gamma = \frac{k_{T,s}}{k_\ell + k_{T,s}} \tag{A12}$$

The laminar fluctuation diffusivity, to be added to the eddy viscosity in the diffusive terms of the momentum and energy equations is given by:

$$\mu_\ell = c_{\mu,\ell} f_{\mu,\ell} \rho \left(\frac{\Omega y^2}{U} \right) \sqrt{k_\ell}, \quad f_{\mu,\ell} = 1 - e^{R_T^{2.5}}, \quad R_T = \frac{\rho k}{\mu \omega} \tag{A13}$$

where y indicates the distance from the nearest wall, Ω the vorticity magnitude, U the velocity, S the mean strain rate, k_ℓ the laminar kinetic energy, k the turbulent kinetic energy, μ the fluid dynamic viscosity, μ_ℓ the laminar dynamic viscosity, μ_T the turbulent dynamic viscosity including the shear stress limiter (Menter 1994) and given by:

$$\mu_T = \rho \frac{a_1 k}{\max(a_1 \omega, F_2 S)} \tag{A14}$$

Standard values for the constants are provided by Table 2 and $c_{ss} = 2$.

The inlet condition for the LKE is $k_\ell = 0$. The boundary condition at a wall is $k_\ell = 0$.

Funding Open access funding provided by Università degli Studi di Firenze within the CRUI-CARE Agreement. The University of Florence acknowledges the contribution of ICSC–Italian Research Center on High Performance Computing, Big Data, and Quantum Computing, funded by the European Union–NextGenerationEU (CUP B83C22002830001). Funding from Italian Ministerial grant PRIN 2022 ”Machine-learnt RANS modelling for transitional and turbulent flows based on High-Fidelity simulations and measurements” (MILESTONE) (CUP B53D23006110006) is also gratefully acknowledged.

Declarations

Conflict of interest The authors declare no Conflict of interest.

References

Akolekar, H., Weatheritt, J., Hutchins, N., et al.: Development and use of machine-learnt algebraic reynolds stress models for enhanced prediction of wake mixing in low-pressure turbines. J. Turbomach. (2019). https://doi.org/10.1115/1.4041753

Akolekar, H.D., Waschkowski, F., Zhao, Y., et al.: Transition modeling for low pressure turbines using CFD-driven machine learning. Energies **14**(15), 4680 (2021). https://doi.org/10.3390/en14154680

Akolekar, HD., Waschkowski, F., Pacciani, R., et al.: Multi-Objective Development of Machine-Learnt Closures for Fully Integrated Transition and Wake Mixing Predictions in Low Pressure Turbines. Proceedings of the ASME Turbo Expo 2022 Rotterdam, Netherlands June 13–17 p V10CT32A013, (2022). https://doi.org/10.1115/GT2022-81091

Arnone, A.: Viscous analysis of three-dimensional rotor flow using a multigrid method. ASME J. Turbomach. **116**(3), 435–445 (1994). https://doi.org/10.1115/1.2929430

Arts T, Lambertderouvroit, M., Rutherford, AW.: "Aero-Thermal Investigation of a Highly Loaded Transonic Linear Turbine Guide Vane Cascade. A Test Case for Inviscid and Viscous Flow Computations.". VKI Training Center for Experimental Aerodynamics TN 174, (1990)

Brinkerhoff, J., Yaras, M.: Numerical investigation of transition in a boundary layer subjected to favourable and adverse streamwise pressure gradients and elevated free stream turbulence. J. Fluid Mech. **781**, 52–86 (2015). https://doi.org/10.1017/jfm.2015.457

Chorin, A.J.: A numerical method for solving incompressible viscous flow problems. J. Comput. Phys. **2**, 12–26 (1967). https://doi.org/10.1006/JCPH.1997.5716

Coder, JM., Maughmer, M.: One-Equation Transition Closure for Eddy-Viscosity Turbulence Models in CFD. AIAA Paper 2012-0672 (2012). https://doi.org/10.2514/6.2012-672

Dick, E., Kubacki, S.: Transition models for turbomachinery boundary layer flows: a review. Int. J. Turbomach. Propuls **2**(2), 4 (2017)

Durbin, P.: Perspectives on the phenomenology and modeling of boundary layer transition. Flow Turbul. Combust. **99**, 1–23 (2017). https://doi.org/10.1007/s10494-017-9819-9

Durbin, P.A.: On the k-ϵ stagnation point anomaly. Int. J. Heat Fluid Flow **17**(1), 89–90 (1996). https://doi.org/10.1016/0142-727X(95)00073-Y

Fang, Y., Zhao, Y., Akolekar, H.D., et al.: A data-driven approach for generalizing the laminar kinetic energy model for separation and bypass transition in low- and high-pressure turbines. ASME J. Turbomach. **146**(9), 091005 (2024). https://doi.org/10.1115/1.4065124

Gaster, M.: The Structure and Behaviour of Laminar Separation Bubbles. Tech. rep., Aeronautical Research Council R &M 3595 (1969)

Ge, X., Arolla, S., Durbin, P.: A bypass transition model based on the intermittency function. Flow Turbul. Combust. **93**, 37–61 (2014). https://doi.org/10.1007/s10494-014-9533-9

Jacobs, R.G., Durbin, P.A.: Shear sheltering and the continuous spectrum of the Orr-Sommerfeld equation. Phys. Fluids **10**(8), 2006–2011 (1998). https://doi.org/10.1063/1.869716

Kubacki, S., Simoni, D., Lengani, D., et al.: An extended version of an algebraic intermittency model for prediction of separation-induced transition at elevated free-stream turbulence level. Int. J. Turbomach. Propuls (2020). https://doi.org/10.3390/ijtpp5040028

Lardeau, S., Leschziner, M.A.: Modeling of wake-induced transition in linear low-pressure turbine cascades. AIAA J. **44**(8), 1854–1865 (2006). https://doi.org/10.2514/1.16470

Lardeau, S., Li, N., Leschziner, M.A.: Large Eddy simulations of transitional boundary layers at high free-stream turbulence intensity and implications for RANS modeling. ASME J. Turbomach. **1**(129), 1–7 (2007). https://doi.org/10.1115/1.2436896

Li, Y., Xu, J., Zhang, Y., et al,: A Novel Local-Variable-Based Reynolds-Averaged Navier-Stokes Closure Model for Bypass and Laminar Separation Induced Transition. Physics of Fluids 33(10), (2021). https://doi.org/10.1063/5.0066007

Lopez, M., Walters, D.K.: Prediction of transitional and fully turbulent flow using an alternative to the laminar kinetic energy approach. J. Turbul. **17**(3), 253–273 (2016). https://doi.org/10.1080/14685248.2015.1062509

Lou, W., Hourmouziadis, J.: Separation bubbles under steady and periodic-unsteady main flow conditions. ASME J. Turbomach. **122**(4), 634–643 (2000). https://doi.org/10.1115/1.1308568

Mayle, R., Schulz, A.: The path to predicting bypass transition. ASME J. Turbomach. **119**(3), 405–411 (1997). https://doi.org/10.1115/1.2841138

Menter, F.R.: Two-equation Eddy-Viscosity turbulence models for engineering applications. AIAA J. **32**(8), 1598–1605 (1994). https://doi.org/10.2514/3.12149

Menter, F.R., Langtry, R.B., Likki, S.R., et al.: A correlation-based transition model using local variables - part i: model formulation. J. Turbomach. **128**(7), 413–422 (2006). https://doi.org/10.1115/1.2184352

Menter, F.R., Smirnov, P.E., Liu, T., et al.: A one-equation local correlation-based transition model. Flow Turbul. Combust. **95**, 583–619 (2015)

Michálek, J., Monaldi, M., Arts, T.: Aerodynamic performance of a very high lift low pressure turbine airfoil (t106c) at low reynolds and high mach number with effect of free stream turbulence intensity. ASME J. Turbomach. **134**(6), 061009 (2012). https://doi.org/10.1115/1.4006291

Michelassi, V., Chen, L.W., Pichler, R., et al.: Compressible Direct numerical simulation of low-pressure turbines - part II: effect of inflow disturbances. ASME J. Turbomach. **137**(7), 071005 (2015). https://doi.org/10.1115/1.4029126

Pacciani, R., Marconcini, M., Arnone, A., et al.: A CFD Study of Low Reynolds Number Flow in High Lift Cascades. Proceedings of the ASME Turbo Expo 2010 Glasgow, UK June 14–18 7:1525 – 1534, (2010). https://doi.org/10.1115/GT2010-23300

Pacciani, R., Marconcini, M., Arnone, A., et al.: An assessment of the laminar kinetic energy concept for the prediction of high-lift, low-reynolds number cascade flows. P I Mech. Eng. A-J Pow. **225**(7), 995–1003 (2011). https://doi.org/10.1177/09576509114124

Pacciani, R., Marconcini, M., Fadai-Ghotbi, A., et al.: Calculation of high-lift cascades in low pressure turbine conditions using a three-equation model. ASME J. Turbomach. **133**(3), 031016 (2011). https://doi.org/10.1115/1.4001237

Pacciani, R., Rubechini, F., Arnone, A., et al.: Calculation of steady and periodic unsteady blade surface heat transfer in separated transitional flow. ASME J. Turbomach. **134**(6), 061037 (2012). https://doi.org/10.1115/1.4006312

Pacciani, R., Marconcini, M., Arnone, A., et al.: Predicting high-lift low-pressure turbine cascades flow using transition-sensitive turbulence closures. ASME J. Turbomach. (2014). https://doi.org/10.1115/1.4025224

Pacciani, R., Marconcini, M., Arnone, A.: Comparison of the AUSM^{+}-up and Other Advection Schemes for Turbomachinery Applications. Shock Waves **29**(5), 705–716 (2019)

Pacciani, R., Marconcini, M., Arnone, A., et al.: Improvements in the prediction of steady and unsteady transition and mixing in low-pressure turbines by means of marchine-learnt closures. ASME J. Turbomach. **146**(5), 051009 (2024). https://doi.org/10.1115/1.4064312

Pironneau, O., Rodi, W., Ryhming, I.L., et al.: Numerical Simulation of Unsteady Flows and Transition to Turbulence. Cambridge University Press, Cambridge (1992)

Rosenzweig, M., Giaccherini, S., Pinelli, L., et al.: Best-Practice Guidelines for High-Fidelity Simulations Based on Detailed Analysis of a Highly-Loaded Low-Pressure Turbine Cascade. Proceedings of the ASME Turbo Expo 2023 Boston, MA, USA June 26–30 p V13BT30A021, (2023). https://doi.org/10.1115/GT2023-102697

Sandberg, R.D., Michelassi, V.: The current state of high-fidelity simulations for main gas path turbomachinery components and their industrial impact. Flow Turbul. Combust. **102**, 797–848 (2019). https://doi.org/10.1007/s10494-019-00013-3

Sandberg, R.D., Michelassi, V., Pichler, R., et al.: Compressible direct numerical simulation of low-pressure turbines - part I: methodology. ASME J. Turbomach. **137**(5), 051011 (2015). https://doi.org/10.1115/1.4028731

Segui, L., Gicquel, L., Duchaine, F., et al.: LES of the LS89 Cascade: Influence of Inflow Turbulence on the Flow Predictions. 12th European Conference on Turbomachinery Fluid Dynamics & Thermodynamics, April 3-7, Stockholm, Sweden, (2017). https://doi.org/10.29008/ETC2017-159

Somers, DM.: Design and Experimental Results for the S809 Airfoil. Tech. rep., NREL/SR-440-6918, (1997).https://doi.org/10.2172/437668

Walters, D.K., Cokljat, D.: A three-equation eddy-viscosity model for Reynolds-averaged Navier–Stokes simulations of transitional flow. J. Fluids Eng. **130**(12), 121401 (2008). https://doi.org/10.1115/1.2979230

Walters, D.K., Leylek, J.H.: A new model for boundary layer transition using a single-point RANS approach. ASME J. Turbomach. **126**(1), 193 (2004). https://doi.org/10.1115/1.1622709

Wheeler, A.P.S., Sandberg, R.D., Sandham, N.D., et al.: Direct numerical simulations of a high-pressure turbine vane. ASME J. Turbomach. **138**(7), 071003 (2016). https://doi.org/10.1115/1.4032435

Wilcox, D.C.: Turbulence Model. CFD, 3rd edn. DCW Industries Inc., La Canada, USA (2006)

Authors and Affiliations

Roberto Pacciani[1] · **Yuan Fang**[2] · **Leonardo Metti**[1] · **Michele Marconcini**[1] · **Richard Sandberg**[2]

✉ Michele Marconcini
michele.marconcini@unifi.it

Roberto Pacciani
roberto.pacciani@unifi.it

Yuan Fang
yuanfang1@student.unimelb.edu.au

Leonardo Metti
leonardo.metti@unifi.it

Richard Sandberg
richard.sandberg@unimelb.edu.au

[1] Department of Industrial Engineering, University of Florence, Via di S. Marta 3, 50139 Florence, Italy

[2] Department of Mechanical Engineering, University of Melbourne, Melbourne 3010, Australia